

Lawrence Berkeley National Laboratory

Recent Work

Title

Close Observation of Hydraulic Fracturing at EGS Collab Experiment 1: Fracture Trajectory, Microseismic Interpretations, and the Role of Natural Fractures

Permalink

<https://escholarship.org/uc/item/65s060bv>

Journal

Journal of Geophysical Research: Solid Earth, 126(7)

ISSN

2169-9313

Authors

Fu, P
Schoenball, M
Ajo-Franklin, JB
[et al.](#)

Publication Date

2021-07-01

DOI

10.1029/2020JB020840

Peer reviewed

JGR Solid Earth



RESEARCH ARTICLE

10.1029/2020JB020840

Key Points:

- A suite of intermediate-scale hydraulic fracturing experiments in a highly instrumented testbed are presented
- Microseismicity, distributed temperature, and direct wellbore observations reveal fracture propagation and interaction behaviors
- An open natural fracture interacts with hydraulic fracture in complex ways while mineral-filled fractures do not actively participate

Supporting Information:

Supporting Information may be found in the online version of this article.

Correspondence to:

P. Fu,
fu4@llnl.gov

Citation:

Fu, P., Schoenball, M., Ajo-Franklin, J. B., Chai, C., Maceira, M., Morris, J. P., et al. (2021). Close observation of hydraulic fracturing at EGS Collab Experiment 1: Fracture trajectory, microseismic interpretations, and the role of natural fractures. *Journal of Geophysical Research: Solid Earth*, 126, e2020JB020840. <https://doi.org/10.1029/2020JB020840>












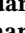




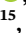


Received 24 AUG 2020

Accepted 25 JUN 2021

© 2021. The Authors.

This is an open access article under the terms of the [Creative Commons Attribution-NonCommercial License](https://creativecommons.org/licenses/by-nc/4.0/), which permits use, distribution and reproduction in any medium, provided the original work is properly cited and is not used for commercial purposes.

Close Observation of Hydraulic Fracturing at EGS Collab Experiment 1: Fracture Trajectory, Microseismic Interpretations, and the Role of Natural Fractures

Pengcheng Fu¹ , Martin Schoenball² , Jonathan B. Ajo-Franklin^{2,3} , Chengping Chai⁴ , Monica Maceira⁴, Joseph P. Morris¹, Hui Wu¹ , Hunter Knox⁵, Paul C. Schwering⁶, Mark D. White⁵ , Jeffrey A. Burghardt⁵ , Christopher E. Strickland⁵, Timothy C. Johnson⁵ , Vince R. Vermeul⁵, Parker Sprinkle⁵ , Benjamin Roberts⁵, Craig Ulrich², Yves Guglielmi² , Paul J. Cook², Patrick F. Dobson² , Todd Wood², Luke P. Frash⁷ , Lianjie Huang⁷, Mathew D. Ingraham⁶ , Joseph S. Pope⁶, Megan M. Smith¹, Ghanashyam Neupane⁸ , Thomas W. Doe⁹, William M. Roggenthen¹⁰, Roland Horne¹¹ , Ankush Singh¹¹ , Mark D. Zoback¹¹ , Herb Wang¹², Kate Condon¹², Ahmad Ghassemi¹³ , Hao Chen¹⁴, Mark W. McClure¹⁵, George Vandine¹⁶, Douglas Blankenship⁶, Timothy J. Kneafsey² , and EGS Collab Team¹⁷

¹Lawrence Livermore National Laboratory, Atmospheric, Earth, and Energy Division, Livermore, CA, USA, ²Energy Geosciences Division, Lawrence Berkeley National Laboratory, Berkeley, CA, USA, ³Earth, Environmental and Planetary Sciences, Rice University, Houston, TX, USA, ⁴Oak Ridge National Laboratory, Oak Ridge, TN, USA, ⁵Energy and Environment Directorate, Pacific Northwest National Laboratory, Richland, Washington, USA, ⁶Sandia National Laboratories, Albuquerque, NM, USA, ⁷Los Alamos National Laboratory, Los Alamos, NM, USA, ⁸Idaho National Laboratory, Idaho Falls, ID, USA, ⁹Golder Associates Inc., Redmond, WA, USA, ¹⁰Department of Geology and Geological Engineering, South Dakota School of Mines and Technology, Rapid City, SD, USA, ¹¹Stanford University, Stanford, CA, USA, ¹²The University of Wisconsin-Madison, Madison, WI, USA, ¹³Mewbourne School of Petroleum and Geological Engineering, The University of Oklahoma, Norman, OK, USA, ¹⁴Department of Statistics, The University of California, Davis, CA, USA, ¹⁵ResFrac Corporation, Palo Alto, CA, USA, ¹⁶Sanford Underground Research Facility, Lead, SD, USA, ¹⁷The author details of EGS Collab Team are mentioned in the Appendix A

Abstract Despite the wide application of hydraulic fracturing in enhanced geothermal system (EGS) development and unconventional hydrocarbon production, our understanding of the many factors affecting the propagation of hydraulic fractures has relied on circumstantial evidence. This is partly due to the scarcity of direct observations in the subsurface. The EGS Collab project attempts to address these issues in the context of EGS research by performing intermediate-scale (~10 m) hydraulic stimulation experiments in a thoroughly characterized and heavily instrumented underground testbed. This paper analyzes the data collected from the first suite of hydraulic fracturing tests in this testbed, consisting of seven stimulation episodes. High-quality microseismic data delineate five planar features very clearly. Combining fracture-wellbore intersection observations from distributed temperature sensing (DTS) and visual observations from an open-hole well, as well as prior in-situ stress measurements, we conclude with high certainty that the four larger planes were hydraulic fractures. The growth of the hydraulic fractures was temporarily halted by a prominent, open natural fracture in the testbed but they eventually crossed and slightly reoriented under continued stimulation. Mineral-filled (i.e., healed) natural fractures, though prevalent in the testbed, did not have perceivable effects on hydraulic fracture propagation. The high-quality, mutually corroborating data sets allowed conclusions to be drawn with high confidence and attests to the advantage of intermediate-scale experiments in subsurface research.

Plain Language Summary Hydraulic fracturing is a critical process enabling enhanced geothermal system (EGS) development and unconventional hydrocarbon production. Because direct observation in the subsurface is difficult and scarce, our understanding of the many factors affecting the propagation of hydraulic fractures remains vague or unreliable. The EGS Collab project attempts to address these issues in the context of EGS research by performing intermediate-scale (~10 m) hydraulic stimulation experiments in a thoroughly characterized and heavily instrumented underground testbed. In this paper, we analyzed the data collected from the first suite of hydraulic fracturing tests in this testbed, consisting of seven stimulation episodes. High-quality microseismic data delineate five planar features

very clearly. Thanks to the many types of data corroborating each other, we conclude with high certainty that the four larger planes were hydraulic fractures. The growth of the hydraulic fractures was temporarily halted by a prominent, open natural fracture in the testbed but they eventually crossed and slightly reoriented under continued stimulation. Mineral-filled natural fractures, though prevalent in the testbed, did not have perceivable effects on hydraulic fracture propagation.

1. Introduction

Hydraulic fracturing (Hubbert & Willis, 1957) plays a central role in many subsurface processes, particularly in enhanced geothermal systems (EGS) (Brown et al., 2012) and unconventional oil and gas production from shale plays (e.g., Warpinski et al., 2009). In both applications, hydraulic fracturing is responsible for creating fluid conduits in rocks that are otherwise too impermeable to allow for economic development of these resources. Although the extensive application of hydraulic fracturing in unconventional hydrocarbon production has generated tremendous economic impact, our understanding of this process as well as its design and deployment has largely relied on circumstantial evidence. This situation poses an enormous challenge to the research and development of EGS. Many characteristics of fracture growth in shale formations, such as contained height growth, are likely caused by the layered fabrics of sedimentary rocks (Fisher & Warpinski, 2012; Fu et al., 2019). These effects cannot be extrapolated to crystalline rocks, the host rock of typical EGS, which lack the layered structure. While contemporary large-scale shale oil/gas developments can afford to develop a standard fracturing design through a trial-and-error process that yields economic, though not necessarily optimal, production, the limited scale and budget of EGS research demands a more predictive approach rooted in fundamental understanding of subsurface processes such as hydraulic fracture stimulation and fracture flow (McClure & Horne, 2014; US DOE, 2019).

Among the many factors affecting hydraulic fracture behavior, the interaction with natural fractures is a particularly important one. Natural fractures are ubiquitous in rock formations (Bonnet et al., 2001). For shale oil and gas production, it has been speculated that the activation of natural fracture networks, presumably energized by pressurized fluid from hydraulic fractures, is a major, if not the predominant factor in production enhancement (Engelder et al., 2009; Gale et al., 2007, 2017). For EGS, many field experiments have sought to hydraulically stimulate the natural fracture system without creating extensive hydraulic fractures based on the “hydro-shearing” concept (Genter et al., 2010; Willis-Richards et al., 1996). However, an analysis of historical injection data suggested that hydraulic fractures were actually generated in nearly all cases, perhaps resulting in a “mixed-mechanism stimulation” (McClure & Horne, 2014). The perceived predominant role of natural fractures has been a dictating theme in the past decade in developing numerical models for hydraulic fracturing (Fu et al., 2013; McClure et al., 2016; Settgast et al., 2017; Weng et al., 2011; Zhang et al., 2009). However, evidence from recent core-back experiments have called some of the prevailing notions into question. In the Eagle Ford formation in Texas (Raterman et al., 2018), natural fractures are scarce while an unexpectedly large number of hydraulic fractures were observed in cores, likely the main factor contributing to permeability enhancement. In the Midland Basin of Texas, cores from the Hydraulic Fracture Test Site (HFTS) experiment (Ciezobka et al., 2018) revealed a large quantity of natural fractures and hydraulic fractures but did not show extensive interactions between the two types of fractures (Gale et al., 2018, 2019).

The difficulty in directly observing hydraulic fractures at relevant depths is a main factor contributing to the aforementioned deficiency in the understanding of hydraulic fracture behavior. While microseismic imaging is the most widely used technique for inferring the propagation patterns of hydraulic fractures (Maxwell et al., 2010), what the so-called microseismic “clouds” (Shapiro et al., 2006) signify, i.e., whether being the actual footprints of the fractures or the extents of the resultant stress/pressure perturbations, remains a matter of debate (Riffault et al., 2018; Shapiro & Dinske, 2009; Sherman et al., 2019). The aforementioned “core-back” experiments in the Eagle Ford formation (Raterman et al., 2018) and in the Midland Basin (Ciezobka et al., 2018), as well as the earlier Multiwell Experiment Site in Colorado (Warpinski et al., 1993), cored through hydraulic fractures and thereby enabled direct observation of fracture characteristics. However, such experiments only sample a very small area of each fracture that the well intersects and therefore only provide very limited information about fracture growth and interactions. “Mine-back” experiments can directly expose traces of fractures and fracture intersections (Fisher & Warpinski, 2012; Jeffrey et al., 2009), and thereby provide unique insights. However, existing mine-back experiments were

Table 1
A Summary of Key Data Used in This Study

Data	Section	Figure and Table	Supporting information
Testbed design; well naming	2.1	Figure 1	Well trajectory 3D model in Data Set S4
Natural fractures: fracture types, orientations, and one prominent fracture	2.2	Figures 1, 2, and 12	Natural fracture catalog in Data Set S1
Pumping configuration/schedule	3.1	Figures 3 and 5; Table 2	Raw stimulation data available at https://gdr.openei.org/submissions/1229
DTS observations	3.2	Figures 4 and 5	Full DTS data set in S3
Water jetting observations	3.3	Figures 5–8	Movie S1, S2; full footage available at https://gdr.openei.org/submissions/1227
Microseismic events	4	Temporal: Figures 3 and 11; spatial: Figures 9 and 10	Event catalog in Data Set S2; 3D model of fitted fracture planes in Data Set S5; Movie S3

not subjected to extensive “close-range” geophysical monitoring, and the 3D visibility is limited by the surface of excavation. Intermediate-scale field experiments, involving fractures tens of meters in size, offer information complementary to full-size field studies and laboratory-scale experiments. Such experiments can also engage fracturing processes with length-scales, time scales, and in-situ stress conditions relevant to field applications. The relatively easy access to the testbed from underground openings makes it possible to deploy extensive close-range monitoring systems with thorough spatial coverage to make observations and measurements that are infeasible for both lab-scale and full field-scale experiments (Dutler et al., 2019; Krietsch et al., 2018, 2019; Zang et al., 2017).

The current paper reports and analyzes data collected from the first suite of hydraulic stimulation experiments at the EGS Collab project, an ongoing intermediate-scale EGS-focused field experiment (Kneafsey et al., 2020). We focus on two aspects of the experiment results:

1. To investigate the fracture trajectories and their relationship with microseismic observations
2. To investigate the influence of natural fractures on the propagation of hydraulic fractures

The paper uses a data set including several types of data collected in EGS Collab Experiment 1. In Sections 2–4, we first present these data and perform basic analyses on individual data types. Section 2 presents the design and setup of the EGS Collab testbed as well as the natural fractures mapped in the testbed. Section 3 presents the stimulation history and some direct observations made during the stimulations, including temperature anomalies observed along the wellbores and water jetting visible in one of the wells. Section 4 presents the microseismic data, based on which several stimulated hydraulic fractures were identified. We combine all the above data in Section 5 to perform comprehensive analyses regarding the two key questions presented above. Table 1 summarizes the main data used in this work and maps them to various components of the paper. Note that a recent paper by Schoenball et al. (2020) was based on the same broad EGS Collab data set, and the scope of that paper overlaps with the present paper to some extent. The relationship and differences between of the two papers are discussed in Supporting Information Text S1.

2. EGS Collab Experiment 1 Testbed

2.1. Testbed Design

The testbed of EGS Collab Experiment 1 was constructed at SURF (Sanford Underground Research Facility), formerly the Homestake Gold Mine, in South Dakota, USA at a nominal depth of 4,850 ft (1,478 m) below ground surface (Heise, 2015). The testbed is located within the West Access Drift of the “4,850 ft level” in the phyllite of the Precambrian Poorman Formation (Caddey et al., 1991). Multiple in-situ stress measurements had been performed in a nearby vertical well as a part of the KISMET experiment (Oldenburg et al., 2016; Wang et al., 2017). For Collab Experiment 1, two circulation wells (nominally injection and production, respectively) and six monitoring wells were drilled from the drift, as illustrated in Figure 1. All wellbores have a nominal diameter of 96 mm or 4 in. The injection well (E1-I) was drilled along a nominal direction of N4°W with a 12° down dip, which was the average minimum principal stress (S_{hmin}) direction

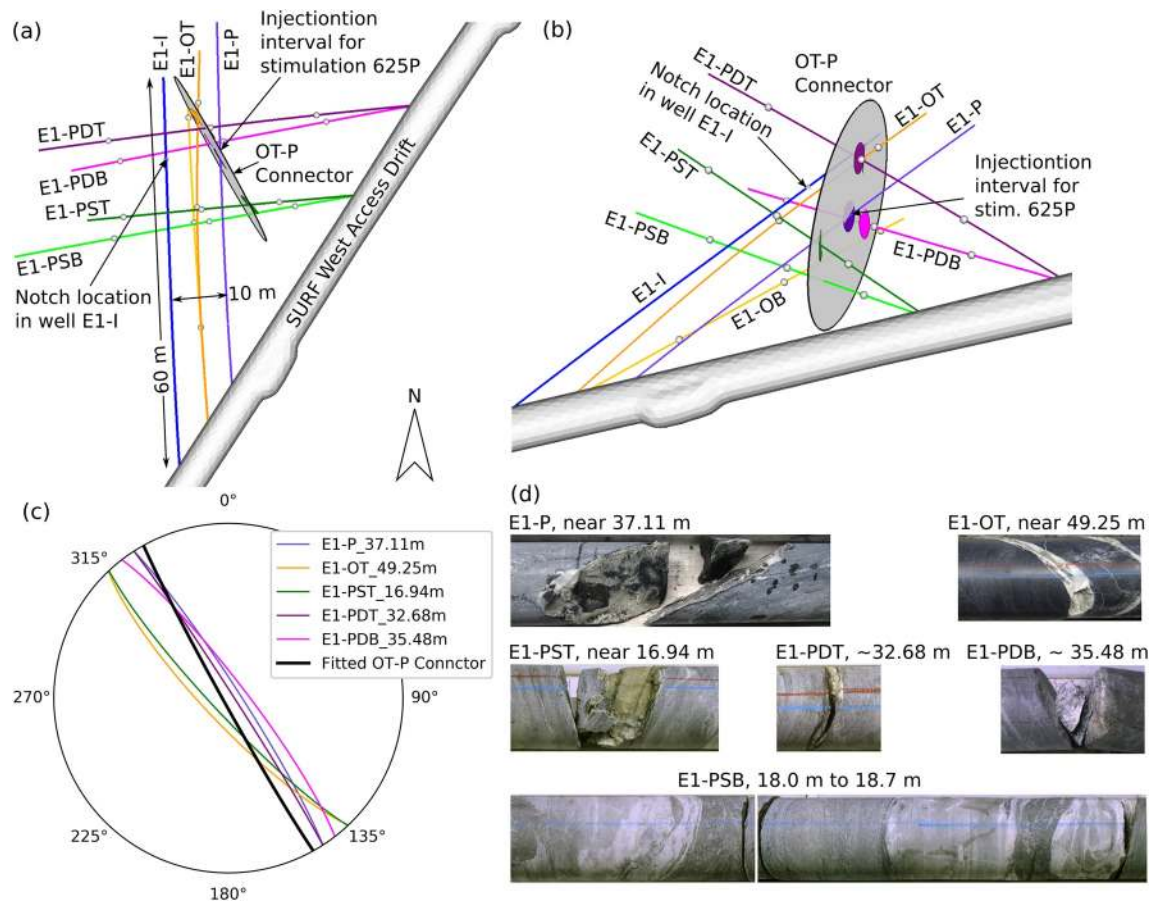


Figure 1. The EGS Collab Experiment 1 testbed, including the SURF 4,850 ft level West Access Drift, the eight wellbores, and a fitted plane to represent the “OT-P Connector” as presented in Section 2.2, in (a) plan view and (b) side view. The size of OT-P Connector is nominal as there is no data to constrain its extents. The well trajectories were measured in a gyro survey and therefore slightly deviate from the designed straight lines. (c) Lower hemisphere stereographic projections of traces of OT-P Connector visible in five wells (E1-P, E1-OT, E1-PST, E1-PDT, E1-PDB), with the intersection depths denoted in the legend. The orientations of these five intersections are shown in (a) and (b) as small disks colored the same as the corresponding wells. The stereonet projection of the fitted OT-P Connector is shown as a thick black line. (d) Core segments corresponding to the five intersections. Cores from a sixth well, E1-PSB, near the projected intersection between this well and OT-P Connector are also shown although no corresponding fractures were logged in this well at this location.

based on mini-fracturing tests in KISMET, as interpreted at the time of designing Collab’s testbed. Note that a reinterpretation after Collab’s testbed had been built yielded a S_{hmin} orientation of N33°E with a 9° down dip. Because the drift axis is oriented N33.5°E, the angle between the stimulation well axis and the drift axis is 37.5° in a plan view. The production well (E1-P) is parallel to well E1-I, ~10 m to the east to intercept the generated hydraulic fractures. Both E1-I and E1-P used an open-hole design, and SIMFIP (Step-rate Injection Method for Fracture In-situ Properties) (Guglielmi et al., 2014) measurements were made in these two wells during selected stimulations. Six “fracture notches” in the form of ring-shaped grooves with sharp edges were cut in E1-I using a specially fabricated mechanical tool to allow transverse hydraulic fractures to initiate from these designated locations. All the stimulations described here involved injecting through a straddle packer assembly with a 1.64 m long open-hole interval centered at the fracture notch at 50.2-m (164 ft) depth. Note that perforation holes created by shape charges as commonly used in the field to facilitate the initiation of hydraulic fractures were not used here for safety considerations. It is possible that fractures initiated from these two mechanisms (i.e., notches and perforations) are different in certain aspects, but the differences are expected to be limited to a distance several times of the diameter of the wellbore. The processes discussed in the current work took place in much farther distances to the wellbore.

As the injection well was drilled along the estimated S_{hmin} direction, the hydraulic fractures to be initiated from E1-I were expected to be largely perpendicular to the injection well. Predesign modeling work (Fu

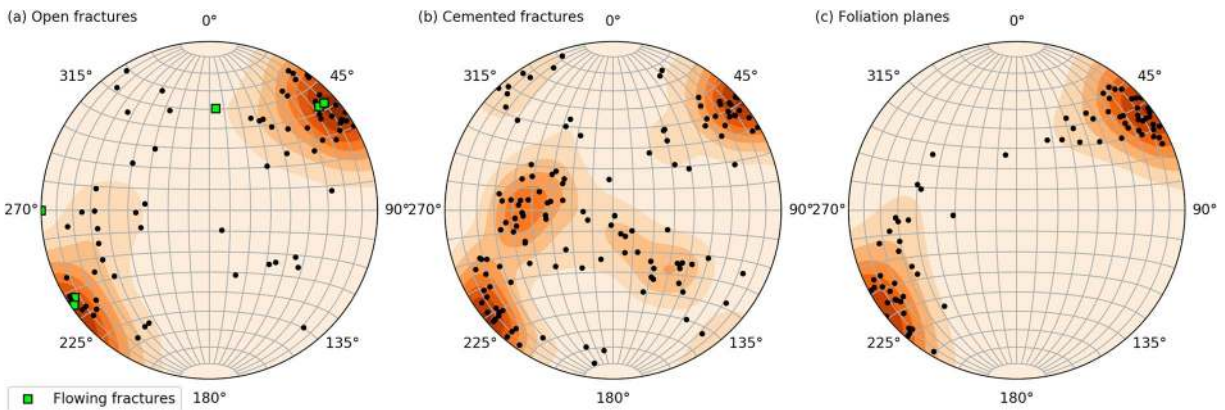


Figure 2. Lower hemisphere pole plots, including density contours of the orientations of fractures and foliation planes logged in the eight wells. In (a), the five “flowing fractures” are denoted by green squares. The natural fracture catalog is included in the Supporting Information.

et al., 2018) found that the many decades of cooling of the rock surface due to mining activities has generated thermal stress around the drift. At the center of the testbed, ~40 m from the drift, the magnitude of the thermal stress perturbation is ~1 MPa of reduction in compression. This is only a small fraction of the differences between principal in-situ stresses, which are estimated to be at least 15 MPa. Therefore, the thermal stress does not have a substantial effect on the orientation of the in-situ stress. As the kISMET mini-fracturing tests were performed between 40 and 100 m below the drift, the thermal stress should not have significantly affected the in-situ stress orientation measured by those tests either. The gradient of the thermal stress perturbation in the direction radial to the drift axis is 10’s kPa/m at the center of the test bed. This is enough to create a strong tendency for a hydraulic fracture to propagate toward the drift.

Several monitoring wells were drilled from the drift, four parallel to the expected fracture plane and two orthogonal to the expected fracture plane to provide thorough coverage of the testbed. The four parallel monitoring wells are named E1-PST, E1-PSB, E1-PDT, and E1-PDB, respectively, with “P” denoting “parallel,” “S” denoting “shallow,” “D” denoting “deep” in terms of the distance to the wellhead of E1-I, “T” denoting “top,” and “B” denoting “bottom.” The other two are named E1-OT and E1-OB, respectively, with “O” denoting “orthogonal.” Multiple geophysical methods including continuous active-source seismic monitoring (CASSM) (Ajo-Franklin et al., 2011; Daley et al., 2007, 2011), microseismic (MEQ), electrical resistivity tomography (ERT) (Johnson et al., 2012), and continuous distributed monitoring of temperature (DTS), seismic wavefield as measured by strain rate (DAS), and strain (DSS) using fiber-optic cable were employed in these observation wells. The locations of three-component accelerometers are shown in Figure 1. The deployment of geophones, hydrophones, and other sensors is described in Schoenball et al. (2020). A fiber-optical cable ran through the entire lengths of all the six observation wells; a more detailed description of the DTS system is provided in Section 3.2. Although these wells were intended to house sensors and cables, it is still possible for the hydraulic fractures to intersect them and for fluid to flow into and eventually flow out from the wellheads.

2.2. Natural Fractures and Initial Saturation in the Testbed

Based on wellbore televiewer log images and the continuous cores retrieved from the eight wells (466.7 m in total length), 206 intersections between wellbores and natural fractures were identified in the testbed (Schwering et al., 2020; catalog of these fractures are included in the Supporting Information). All cores were retrieved during the original drilling; no core-back was performed after the experiments. Note that a fracture could intersect multiple wells and be logged multiple times. The Collab team classified the fractures into three categories: (1) naturally “flowing fractures,” from or into which water can flow freely at a pressure close to the atmospheric pressure; (2) visually “open fractures,” with partially open aperture but no significant hydraulic conductivity under low pressure; and (3) “cemented fractures” (i.e., mineral-filled or healed) without apparent opening or hydraulic conductivity and sealed by mostly quartz or calcite. There were 5, 71, and 130 fractures identified in these three categories, respectively. Figures 2a–2c show lower

Table 2
Summary of the Stimulation Activities Concerned in the Current Work

Label	Date, in 2018	Stim. well	Duration (min) at rate >0.05 L/min	Max. flow rate (L/min)	Total inj. vol. (L)
522	May 22	E1-I	10.5	0.2	2.1
523	May 23	E1-I	65.2	0.4	23.3
524	May 24	E1-I	31.7	5.0	79.6
525A	May 25	E1-I	31.5	4.6	77.8
525B	May 25	E1-I	32	4.6	119.3
625P	June 25	E1-P	7.7	4.4	25.6
625I	June 25	E1-I	80.6 ^a	5.5	170.1

^aDue to the high noise in pumping rate data, the injection rate threshold rate is adjusted to 0.25 L/min for this time window.

hemisphere pole plots of the natural fracture planes as well as density contours of the poles of the fractures. Although the fractures have a wide variety of orientations, the majority of natural fractures are NE-SW striking and steeply dipping, forming a coherent fracture family. Particularly, four of the five “flowing fractures” belong to this family. Additionally, 72 foliation planes were identified from the wellbore images. According to the orientations summarized in Figure 2c, the majority of the foliation planes are NE-SW striking and steeply dipping as well. These observations hint a significant rock fabric dictated by these consistent foliation planes and fracture planes.

A prominent feature of the natural fracture system is that three flowing fracture traces and two open fracture traces in five different wells seem to conform to the same planar structure. Figure 1c shows the orientations and the depths of the five traces as well as the orientation of the best-fit plane (strike 150.9°, dip 87.5°) based on the locations of the traces. The linear-regression fitting yielded a R^2 value (the coefficient of determination) of 0.99. It is highly likely that these five traces belong to the same

open natural fracture as illustrated in Figures 1a and 1b. This natural fracture is referred to as the “OT-P Connector” because fluid injected into the trace in E1-OT under low pressure flows out of the trace in E1-P and vice versa. The five core sections in Figure 1d show that OT-P Connector is partially filled with calcite and quartz of various thicknesses and has partially open aperture of up to several millimeters. Although no open fracture was logged near the projected intersection (~18.5-m deep) between OT-P Connector and well E1-PSB, the cores near that location, shown in Figure 1d, have a thick segment of quartz. Their hydraulic significance of OT-P Connector is further discussed in Wu et al. (2021).

As the rock body is fractured and the drift has experienced a complex history (Fu et al., 2018), the saturation condition of the rock surrounding the drift is speculated to be complicated. The pores and less conductive fractures should be water-saturated, evidenced by the moist rock surface. Large, conductive fractures, including the OT-P Connector are likely to have been drained (i.e., partially air-saturated) near the drift. From the drift to the far field, the pore pressure transitions from approximately atmospheric pressure to native hydrostatic pressure. Quantifying this transition is not concerned in the current work. The rock matrix’s very low permeability is a significant impediment to an accurate measurement. Homogenized bulk permeability (including the effects of smaller natural fractures) is estimated to be in the order-of-magnitude of microdarcies ($\sim 10^{-18} \text{ m}^2$).

3. Hydraulic Stimulations and Observations From Wellbores

3.1. Hydraulic Stimulations

In this study, we discuss the seven episodes of hydraulic stimulation performed between May 22 and June 25, 2018 as summarized in Table 2. They are labeled based on the date of stimulation. All stimulations, with one exception as described below (625P), were focused on the 50-m deep notch in well E1-I. This location is denoted by a “diamond” symbol in all applicable figures.

- Stimulation 522, performed on May 22, 2018, with the intention to initiate a hydraulic fracture from the target notch (50-m deep) and propagate the fracture to a nominal radius of 1.5 m according to calculations and simulations in the design phase
- Stimulation 523 gradually stepped up the pressure and injection rate to propagate the fracture to a nominal radius of 5.0 m
- Stimulation 524 used higher injection rates to further propagate the fracture to connect to well E1-P. Although the rates were >10 times higher than those used in prior stimulations, the absolute value, 5 L/min, is still relatively low. This was not only limited by the capacity of the pumping system, but also based on the design consideration that the stimulated fracture should not propagate across the entire testbed too fast to allow a reasonable observation window. Significant flow was observed out of wells E1-OT and E1-P 10 and 11 min, respectively, after the injection was switched to flow rate-control, indicating

a fracture(s) intersecting these two wells. The injection rate under flow rate-control was initially at 2.6 L/min and increased to 5 L/min when the intersections took place

- Stimulation 525A, the first of the two episodes on May 25, was performed to repeat the injection of stimulation 524 to make additional SIMFIP measurements in two wellbores, E1-I and E1-P. During stimulation 525B, a downhole camera was used to survey well E1-P to enable visual observations of fracture intersections with the well
- On June 25, two stimulations, 625P and 625I, were conducted to interrogate behaviors of the testbed. For stimulation 625P, two relatively short injections were attempted in well E1-P. The packer interval, through which the fluid entered the formation, was between 39.34-m (129.07 ft) and 40.59-m (132.86 ft) deep, the interval that was earlier identified to contain a hydraulic fracture intersection. Approximately 60% of the injected fluid flowed back as the well was vented soon after the injection
- For stimulation 625I, the injection interval still covered the 50-m deep notch. Higher injection rate and larger injection volume were used in an attempt to enhance the connectivity between E1-I and E1-P. The flow rate out of E1-P reached 400 ml/min or ~10% of the injection rate, while the flow rate out of E1-OT reached 200 ml/min. A different pump than the one used in other stimulation episodes was used for stimulation 625I, resulting in high-frequency fluctuations in both the injection rate and injection pressure

The injection rate-pressure histories of these stimulation episodes are plotted in Figure 3. The corresponding microseismic events are plotted in Figure 3 too but will be presented in Section 4. Also shown in the figure are the pressure and flow rate for a few pressure transient tests with low injection rates between June 20 and June 22, 2018, during which no microseismic events were observed.

3.2. Temperature Anomalies Along Wellbores From DTS

Temperature of all the six monitoring wells was continuously monitored via a fiber-based distributed temperature sensing (DTS) system involving a fiber-optic cable that runs through the full lengths of these wells. The fiber-optic cable is a PE jacketed tactical, aramid-packed bundle including four single-mode and four multimode fibers (OCC); measurements were made using a commercial Raman DTS system (XT-DTS, Silixa LLC) calibrated for absolute temperature using the duplexed single-ended approach detailed in Hausner et al. (2011) and two control baths of different temperatures located in the mine drift. A small amount of cross-talk exists between thermostat cycles in the calibration bath and the absolute temperature correction, which yields some temporal artifacts in corrected temperature values but not in uncorrected measurements. DTS data for May and June 2018 from the testbed are included in the Supporting Information.

During stimulations, various temperature anomalies in the form of sudden temperature increases (<2.0 °C) were observed in wells E1-OT and E1-PDB. The recorded sudden temperature increases are believed to be caused by the Joule-Thomson effect and indicate intersections of pressurized fractures with wellbores (Zhang et al., 2018). Note that water in an open/propagating hydraulic fracture is under tens of MPa of pressure. When water enters a wellbore through an intersection between the fracture and wellbore, its pressure rapidly decreases to close to the atmospheric pressure, hence inducing warming of the water due to the Joule-Thomson effect.

Such temperature anomalies appeared in two depths, ~44.5 and 46 m, in well E1-OT. The deeper anomaly first appears at 19:30 UTC (Coordinated Universal Time) on May 23, 2018, in the middle of stimulation 523. This anomaly was also mentioned in Schoenball et al. (2020, Section 3.1), although in that work it was estimated at 47-m deep. The depths used in the current paper were based on newer and more accurate calibrations. Stronger temperature signals were observed at both depths beginning at 22:40 UTC on May 24, during stimulation 524, a few minutes before outflow water was observed at the wellhead of E1-OT. Similar temperature anomalies at both depths were observed in the three subsequent stimulations from E1-I: 525A, 525B, and 625I, but not during 625P when injection occurred in well E1-P. A temperature anomaly at 32.5-m depth in well E1-PDB appeared during stimulation 625P, the only injection episode from E1-P, but not during any stimulation from E1-I. An inspection of wellbore logs and core photos did not reveal any natural fractures in these three locations, so these temperature anomalies are attributed to hydraulic fractures. We will use the locations of these temperature anomalies to corroborate the fracture planes determined from

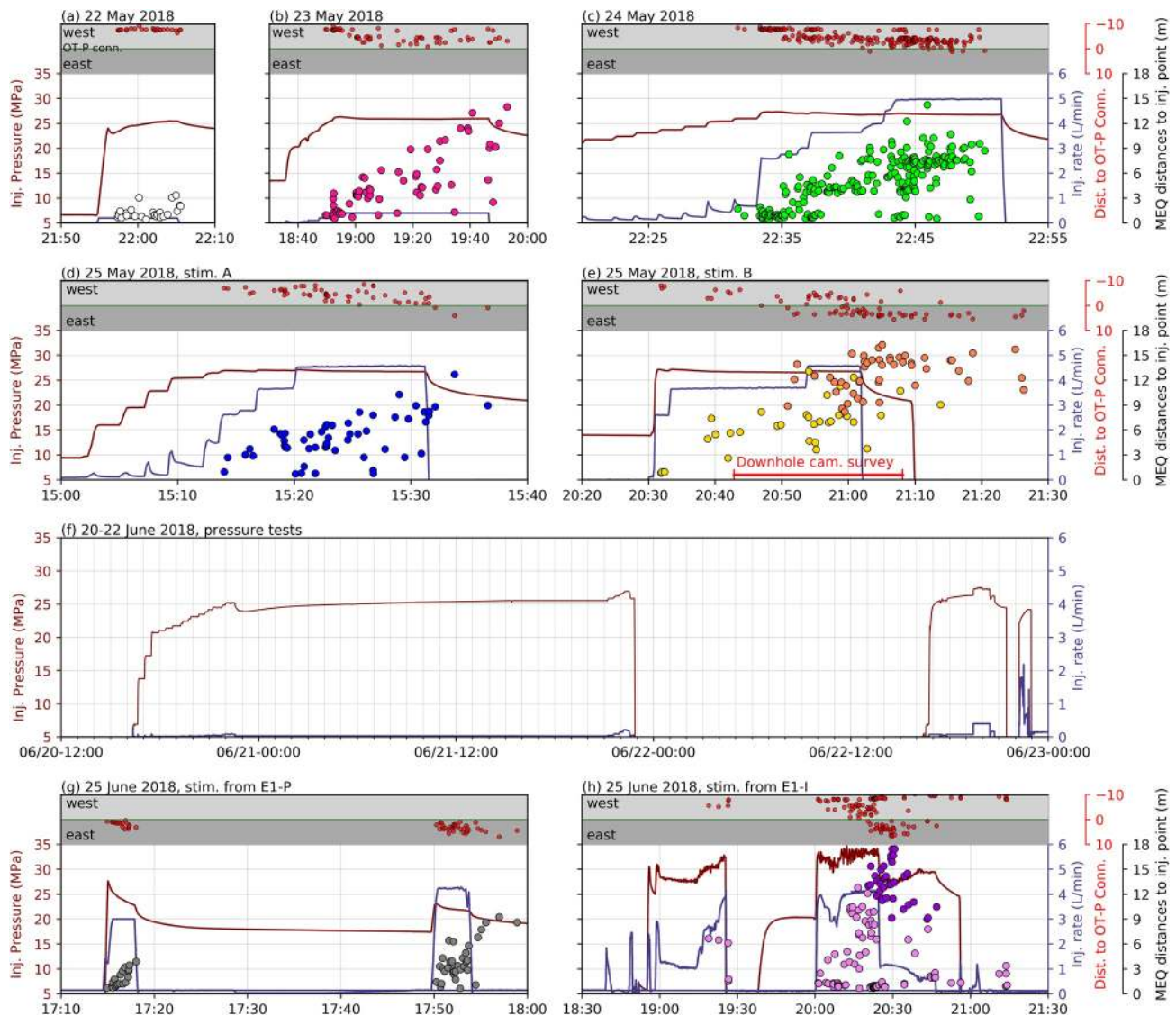


Figure 3. Injection rates and pressure for the seven stimulation episodes (a–e, g, and h) and some pressure transient tests (f) in May and June 2018. In the lower portion of each subfigure except for (f), circles show the times and distances of individual, located microseismic events to the injection points. The colors of circles correspond to those plotted in Figure 9. In each of (e) and (h), two colors are used to differentiate between events west (lighter color) and east (darker color) of the OT-P Connector plane. The distances of the events to the OT-P Connector plane are also visualized in the narrow panel above each plot. Note that stimulation 625P was from well E1-P while the other six episodes were all from the same stimulation segment of E1-I. No microseismic events were detected during the pressure transient tests depicted in (f). Note all dates and times in this paper are in UTC (Coordinated Universal Time).

other data in Section 5.1. Note that the background thermal gradient along each well is caused by cooling at the drift discussed previously.

3.3. Direct Observation of Hydraulic Fractures From Water Jetting

Another direct observation of the hydraulic fracture locations was through a downhole camera survey conducted in well E1-P during stimulation 525B. The survey started at 20:42:50 UTC, ~12 min after the injection had started, and ended at 21:08:06 UTC, 8 min after the termination of the injection. In the first 12 min of the survey, the camera surveyed between 30.5-m (100 ft) and 42.7-m (140 ft) depth, the interval covering the expected intersection with the hydraulic fracture. The only visible response during this first pass was a single thin water “jet” at ~38.75-m (127 ft) depth when the camera passed this location at ~20:46 UTC. A visible increase in downward flow along the wellbore was observed near 42.7-m (140 ft) deep at 20:54 UTC.

Then the camera was moved to resurvey the shallower segment. When the camera arrived at the segment between 38.4-m (126 ft) and 39.6-m (130 ft) deep at 21:01 UTC, a number of “jets” had emerged, spraying water into the wellbore. The camera was moved further upward at 21:04 UTC to survey shallower depths, ~2 min after the injection well E1-I was shut-in. The jets remained active in this 3-min observation window. No jetting activities were visible in shallower depths. The video footage of the survey is included in the Supplementary Materials.

Careful inspection of the downhole camera survey revealed two clusters of water jets, at ~38.8-m (127 ft) and 39.4-m (129 ft) deep, denoted as Cluster 127 and Cluster 129, respectively. Four forms of jets are identified as illustrated in Figure 6. (1) Individual jet streams each consisting of a stream of water were jetting from small vents, such as jets A–H, and K. Some individual jetting points seem to belong to a linear feature, such as jets C, D, and E, as well as jets F, G, and H. Note that although the overall jetting patterns during the observation window were stable, jets from individual vents could emerge and disappear sporadically. Especially, jets from the same apparent linear feature seemed to “take turns” to discharge water from the same source. For instance, of the feature delineated by vents C, D₁, D₂, and E, only D₂ was visible in Figure 6a, C was visible in (b), and D₁, D₂, and E were visible in (c). (2) Jetting slits cause water to jet from a short linear feature, such as slit I denoted in Figure 6f. (3) Dispersed jet groups have individual vents that are closely spaced but do not form an apparently linear feature, such as jet group J in Figure 5d. (4) Bubbling point (L) is results when a jet or a jet group is submerged in water accumulated in the wellbore.

We developed an image analysis technique to precisely locate the jets in the wellbore. First, unwrapped wellbore images of the relevant segment were extracted from optical televiewer logs. The images were enhanced in GIMP (GNU Image Manipulation Program, www.gimp.org) to better distinguish features on the wellbore wall. Then we simulate the view of the downhole camera by virtually wrapping the image and mapping it through a virtual lens. Through this procedure, we obtain a simulated downhole camera view to be compared side-by-side with the corresponding downhole camera image, enabling accurate identification and locating of wellbore features. This method is illustrated in Figure 7 to locate three jets near 39.4-m (129 ft) depth. On the unwrapped wellbore image, the eight jets conform to a sinusoidal curve, indicating that the eight jets are likely along the trace of a plane that intersects the borehole. This plane strikes 108.4° and dips 52.9°N.

The jets near 38.8-m (127 ft) depth are also located following the same procedure and mapped on the unwrapped televiewer well log as shown in Figure 8. Although a plane (127A, shown as the green dashed line) can be found to cut through all the four jets, its orientation is at odds with the apparent orientation of the jet slit I trace. An alternative interpretation is that jets I and K were from the same fracture (127B1) and J and L from 127B2, as illustrated as magenta dashed lines in Figure 8. As two points cannot constrain the orientation of a plane, these two planes were determined so that the angles between the wellbore axis and the planes are maximized. The ambiguity of mapping fractures near the 38.8-m (127 ft) deep interval reflects the complexity of the flow-carrying fracture network near this location, which will be further discussed in Section 5.4. However, it is certain that the thick, cemented natural fracture, although located between jets K and I, was not activated to become a part of the flow-carrying fracture network.

4. Delineating Fractures From Microseismic Monitoring

4.1. Microseismic Data Overview

The microseismic event catalog was generated by a separate but related effort as presented in Schoenball et al. (2020). For detailed information regarding the data acquisition, processing, quality control, and quality evaluation of the microseismic data, please refer to that work. Note that the analyses presented in the current paper are independent of Schoenball et al. (2020). The catalog, as provided as Supporting Information to the current paper, includes 967 events. We first remove the events that are temporally not associated with any of the stimulations, mostly caused by noise from nonstimulation operations in the drift and the wellbores. Among the remainder of the events, those with relatively low estimated location uncertainty based on inversion mismatch tend to form coherent features while many with higher location uncertainty tend to spread randomly in the space. We therefore removed the 25% of the events with the highest calculated location uncertainty. The threshold percentile (25%) was determined somewhat heuristically with a

goal to remove noisy events without undermining any of the features formed by the microseismic events. The remaining 655 microseismic events that occurred within the concerned time windows of the seven stimulation episodes are used to delineate the fracture network resulting from the stimulations. The source locations of these events are visualized in Figure 9 with the colors of the locations representing the corresponding stimulation episodes and whether the locations are to the west or east of OT-P Connector. The events in Figure 3 are also colored using the same mapping rule. To display the complex patterns in the MEQ source locations, Figure 9 shows the same data viewed from four different angles.

4.2. Identifying and Fitting Fracture Planes

Five planar structures can be clearly identified from the microseismic source locations in Figure 9: four larger features, two on each side of OT-P Connector and one small feature near the bottom of the testbed on the west side of OT-P Connector. We assume each of the planar features was associated with a fracture, which is to be substantiated in Section 5. We label each fracture using two letters, the first indicating which side it is located with respect to OT-P Connector and the second indicating the relative locations among the features on the same side. The two larger features to the west are fracture W-N and fracture W-S, and the small lower one fracture W-L, with N, S, and L denoting, north, south, and lower, respectively. The two features to the east are fracture E-N and fracture E-S.

We assigned source locations to these fractures through the following manual process. Note that OT-P Connector is a natural dividing plane. It was easy to manually construct a “dividing plane” between the two features to the east of OT-P Connector as the two features are relatively far apart and there were few events in-between. For fracture W-L, we first picked a source location at the visual center of the cluster of events, and this event’s coordinate is (817.44 m, −1297.43 m, 100.702 m). Note that we use the SURF standard coordinate system with x , y , and z axes pointing to east, north, and up, respectively. All source locations within 1.5 m from this center was attributed to fracture W-L; the threshold distance was chosen to maximize the inclusion of events that visually belong to this cluster while avoiding including events on or beyond fracture W-S. The dividing plane between W-N and W-S was manually constructed to be parallel to and in the middle of the two planar features. Source locations within 2 m from well E1-I are excluded as many were caused by disturbances inside the well and near-wellbore complexity, including during the stimulations. The algorithm that we used would attribute each source location to one of the features even when that event is an apparent outlier. Since such outliers are infrequent, including them in the following regression models would not have a major impact on the results.

We then perform linear regression in the form of $y = ax + bz + c$ on coordinates of source locations attributed to each fracture plane to quantify its orientation. The results are shown in Table 3, and the fitted planes are shown in Figure 9, which shows that most planes are associated with events from multiple stimulation episodes (spheres in different colors). We will assess the accuracy of the inferred fracture locations and the implications for fracture stimulation in Section 5.1.

We did not remove outliers that are clearly not associated with any of the five identified fracture planes. In spite of this, the coefficients of determination (R^2) for the regressions are fairly high, indicating the simple model’s ability to capture the main spatial trends in the data. The regression model can assess the uncertainty in the locations of the fitted plane. To visualize such uncertainty, we use the fitted models to predict the 95% confidence interval for the y coordinates corresponding to the (x, z) coordinates along the manually determined perimeters of the five fracture planes. Such intervals are visualized as semitransparent disk-shaped boxes as shown in Figure 10. The thicknesses of the disks vary between 0.2 and 0.6 m, depending on the scattering of the microseismic events near each location. As the 95% confidence intervals are much smaller than the distances between the fractures, it is evident that the fitted planes are indeed discrete planar features.

5. Discussion

5.1. Corroborating the Accuracy of the Fitted Fracture Planes

EGS Collab Experiment 1's heavily instrumented testbed offers a rare opportunity to validate the interpretation of microseismic events through corroborations with other measurements. The planar features delineated from microseismic source locations, presumably fracture planes, intersect several wellbores, making it possible to directly observe the manifestations of these planes from those wellbores. Table 4 lists all the calculated intersections between the fitted planes with wellbores. Note that we only consider the intersections within the finite extents of these planes, as illustrated in Figures 9 and 10. Each fracture plane is represented by four joined quarter-ellipses with the axis lengths manually adjusted to coverage the relevant microseismic source locations.

The three temperature anomalies measured by DTS, two in E1-OT and one in E1-PDB, strongly corroborate three fitted fracture planes (W-N, W-S, and E-S). Although the depths in E1-OT based on DTS are 0.4–0.5 m shallower than those calculated from the fitted plane, the discrepancy is well within the expected measurement error margins of the seismic event locations and registered depths of the fiber-optic cable. The fiber-optical cable deployed in the wellbores was not perfectly straight. A correction factor was applied to the registered depths based on the measured length of the cable in the wellbore, the known turn-around-point at the end of the conveyance pipe, and the length of the wellbore. This correction method is known to be not highly accurate. The DTS data are sampled at 0.25-m intervals. It is more important to note that based on both DTS and plane fitting results, the separation between the subparallel fractures W-N and W-S is ~1.5 m where they intersect E1-OT. The spatial coincidence between the E1-I-W-S intersection and the location of the precut notch (50.2-m deep) could suggest that fracture W-S could have been initiated from that notch, but this is not definitive as the fracture might not be absolutely planar.

5.2. Delineating the Fracture Propagation Processes

Considering the small uncertainty in the regression models and the corroborating evidence discussed in Section 5.1, we argue that the delineated planar features are individual fractures. It is therefore reasonable to rely on the occurrence sequence of the microseismic events to infer the propagation patterns of the fractures. In Figure 11 we revisualize the injection and microseismic data in Figure 3 but use the colors of the dots representing microseismic events to denote the fracture planes they are associated with. The color scheme is the same as that used in Figure 10 to facilitate comparison. In both Figures 3 and 11, it is evident that the distance of the farthest microseismic events to the injection point increased with pumping time, a clear indication of the extension of the fracture(s). Additionally, the following observations and inferences can be made, which will be used in subsequent discussions in Section 5:

- Stimulation episode 522 did not propagate the fracture(s) far enough to enable clear attribution of microseismic events to individual planes
- Stimulation 523 primarily stimulated fracture W-N (red), which is corroborated by the observation in Figure 4 that a temperature anomaly in well E1-OT during this episode only appeared in the deeper (46 m) location
- Fracture propagation was much more complex in stimulation episode 524, which was the first time a relatively high injection rate was used, 10 times higher than in the two earlier episodes. Fracture W-N (red) continued to grow but the microseismic events were less frequent than along fracture W-S (green). Fracture W-L (orange), appearing to be an “offshoot” from W-S according to Figure 9, started to develop after W-S grew to certain size. DTS data in Figure 4 also indicates that fracture W-S intersected E1-OT in this episode while W-N remained active
- Episode 525A continued to develop fractures W-S and W-N while the propagation of W-L seemed to have ceased. Note that although there were a few light blue dots (representing fracture E-S) in Figures 11c and 11d, they were scarce and very close to OT-P Connector, therefore not necessarily indicating the development of fractures to the east of OT-P Connector
- In episode 525B, the main propagation was along fracture E-N (magenta). E-S (light blue) also had some growth, but it did not grow as far as E-N did. Note that E-S intersects well E1-P at 39.6-m (129.9 ft) deep, which happened to be the location of one of the jetting clusters observed during stimulation episode

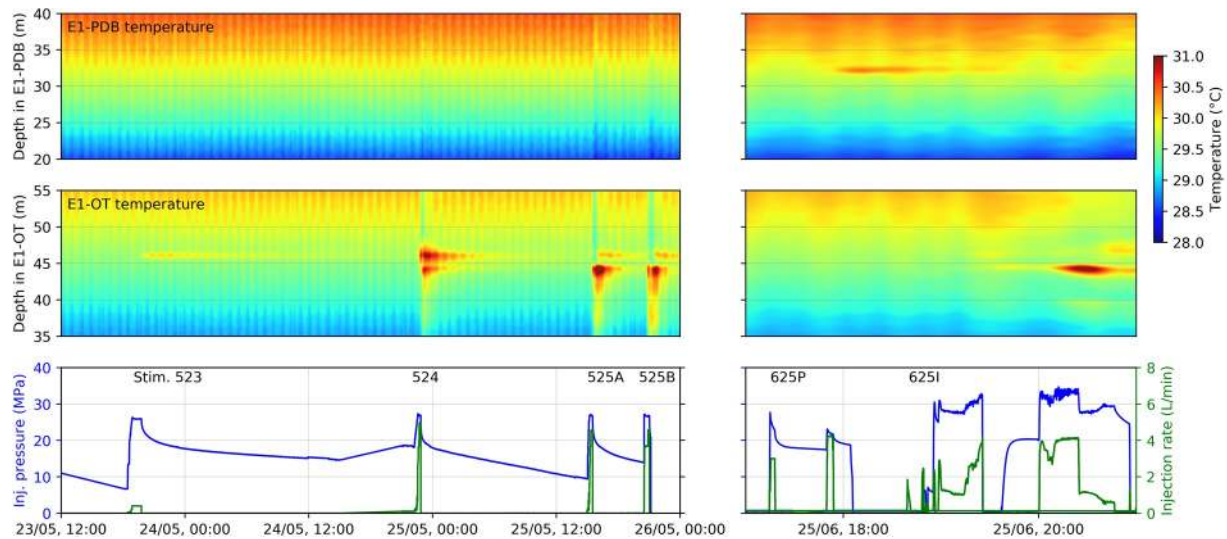


Figure 4. Distributed temperature sensing (DTS) measurement of temperature along well E1-OT and well E1-PDB during the hydraulic stimulations between May 23 and June 25, 2018. “Bicubic” interpolation is used in the DTS plots.

525B. Therefore, the leak-off of fluid through the jets could have negatively affected the growth of fracture E-S

- Episode 625P was the only injection operation into well E1-P. It has been noted previously that the injection interval happened to enclose the 39.4-m (129 ft) deep jetting cluster, which is also the intersection between fracture E-S and well E1-P. Consequently, the main fracture propagation during 625P was along E-S, corroborated by the DTS signal in well E1-PDB at 32.3-m deep, where E-S is expected to intersect this well
- The injection configuration in 625I was similar to that of 525B. It also further propagated W-N, W-S, and E-N, but not W-L or E-S

5.3. The Four Large Planar Features are Likely Hydraulic Fractures

Four relatively large planar features can be discerned from the microseismic cloud (W-N, W-S, E-N, and E-S), two on each side of OT-P Connector. We argue that they are all hydraulic fractures, namely newly created fractures by the water injection through largely tensile failure, as opposed to activated natural fractures. This hypothesis is supported by the following observations:

Observation 1: The fracture planes generally align with independently measured local in-situ stress orientation. The independent measurements were carried out as a part of the kISMET effort (Oldenburg et al., 2016; Wang et al., 2017). In that project, vertical wells were drilled near the wellheads of E1-PDT and E1-PDB. Multiple mini-frac tests were performed in one of the wells at depths between 40 and 100 m, and the orientations of 10 fractures were determined from posttest acoustic televiewer logs. The test configuration dictates that the created hydraulic fractures should be perpendicular to the S_{hmin} direction. These 10 fractures are all consistently east-west trending as illustrated by the lower hemisphere stereographic pole plot in Figure 12a. Note that the orientations of the 10 kISMET fractures as plotted are recently corrected values by the original authors and are therefore slightly different from the values reported in Oldenburg et al. (2016). The orientations of the five fitted fracture planes at EGS Collab Experiment 1 are also plotted for comparison. All five fracture planes are well within the range of variation for the 10 kISMET hydraulic fractures.

Observations 2: No natural fractures coplanar with the four large fractures exist in the testbed. The pole plot in Figure 12b visualizes the relationship between the orientations of the four fitted fracture planes and those of all the natural fractures and foliation planes encountered by the eight wells. Overall, the testbed does not have many east-west trending fractures. In Figures 12c and 12d, we plot all the natural fractures that are

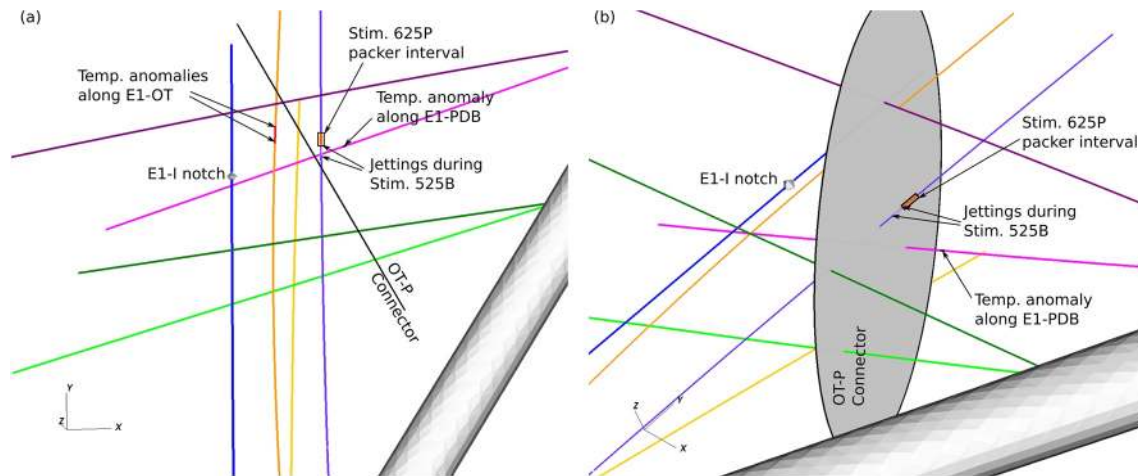


Figure 5. Testbed layout, (a) view from top along prominent natural fracture OT-P Connector and (b) view from the east side, showing locations along wellbores corresponding to observations presented in Section 3 and referred to by subsequent sections. Marked locations include (1) fracture initiation notch at 50-m depth along well E1-I, (2) packer interval (39.34–40.59 m) along E1-P that was injected into during stimulation 625P, (3) two temperature anomalies along E1-OT at 44.5 and 46 m, (4) temperature anomaly along E1-PDB at 32.5 m (active only during stimulation 625P), and (5) jetting locations along E1-P between 38.6 and 39.4 m as observed during stimulation 525B. Note that although interval (2) and interval (5) slightly overlap along E1-P, they were associated with two separate stimulation episodes, respectively. In other words, the jets were not observed when interval (2) was stimulated.

within 10° of the orientations of any of the fitted fracture planes as disks 4.0 m in diameter centered where they are logged along the wellbores. Note that the angle between two planes is defined as $\arccos(\mathbf{n}_1 \cdot \mathbf{n}_2)$, where \mathbf{n}_1 and \mathbf{n}_2 are the unit normal vectors of the two planes. Each disk is colored the same as the fitted fracture plane with which it has a similar orientation. Since the fitted planes have similar orientations among themselves, some natural fractures are within 10° from up to three of the fitted planes. There are five natural fractures within 10° from any of the four fitted planes as shown in Figure 12d, but the offset between each of them and a fitted fracture is quite large. The closest one, the small light blue disk in Figure 12(d), is still 3–4 m laterally offset from fracture E-S. Note that the natural fractures (orange in color) subparallel to fracture W-L are also shown in Figure 12 but we will discuss them in Section 5.5.

Observation 3: None of the water jets observed in well E1-P during stimulation 525B were from any of the natural fractures visible in the televiewer logs, although there were numerous jets and many natural fractures at those locations.

Based on these three observations, we conclude that the four largest fracture planes discerned from microseismic mapping, W-N, W-S, E-N, and E-S, are all new hydraulic fractures instead of natural fractures.

The fracturing pattern that W-N and W-S propagated in a largely parallel fashion with a distance much smaller than the dimensions of the fractures is interesting. The conventional notion is that the so-called stress shadow effect tends to inhibit parallel fracture propagation and generally only one fracture will prevail in the competition leaving the other fractures in its stress shadow (Weng et al., 2011). However, recent observations in field experiments, mostly in the context of shale oil/gas development, have called this notion into question (Gale et al., 2018; Raterman et al., 2018). Although the underlying mechanisms are still under investigation, closely spaced parallel hydraulic fractures have been observed in the few core-back experiments performed up to date. A recent study (Ugueto et al., 2019) that deployed optical fiber in a horizontal well also observed that a “dual peak” signature commonly appeared at many perforation clusters in the poststimulation warm-back DTS measurements. Jeffrey et al. (2009) also saw subparallel strands of hydraulic fracture in a mine-through experiment. These observations, though in different application contexts, all attest the existence of closely spaced parallel hydraulic fractures, which are against the prediction of the stress shadow effect.

It is worth mentioning that the hydraulic fractures initiated from well E1-I predominantly propagated toward the drift. This validates the prediction in Fu et al. (2018) that in this testbed a hydraulic fracture would

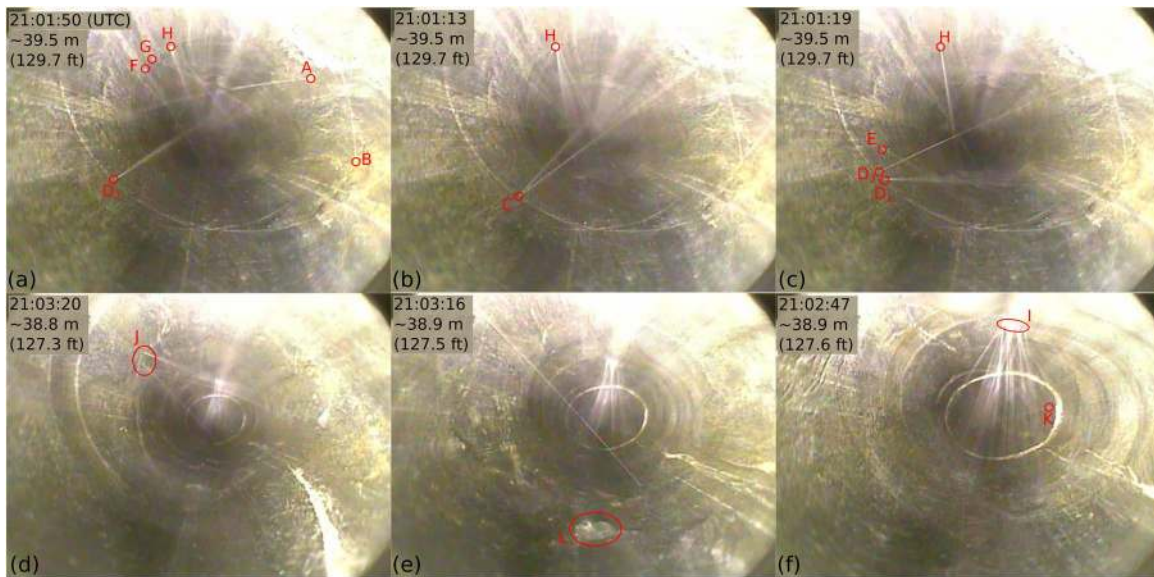


Figure 6. The identification of jetting points based on the downhole camera survey video footage. The wellbore has a nominal diameter of 96 mm or 4 in. (a) to (c) shows the jets near 39.4-m (129 ft) depth in well E1-P and (d) to (f) shows the jets near 38.8-m (127 ft) depth. Small circles denote the points from which individual jet streams originate. Larger ovals denote a jetting slit (I), a jet group (J), and a bubbling spot (L). Note that the linear water stream in (e) originated from group J (out of sight in d) instead of from behind L. The numbers on the upper left corner of each subfigures are the time in UTC and the nominal depth recorded by the downhole camera, which deviated from the true depth calibrated based on wellbore televiewer survey by up to 0.6 m or 2 ft. Selected footages of the downhole camera survey are included in the Supporting Information. Full footages as well as documentation are available at <https://gdr.openei.org/submissions/1227>.

have a strong tendency to propagate toward the drift as dictated by the gradient of S_{hmin} caused by cooling induced by the drift.

5.4. The Role of Natural Fractures: OT-P Connector

The influence of OT-P Connector, the most prominent natural fracture in the testbed with a variable yet overall quite large aperture, on the propagation of the hydraulic fractures is clearly visible in the microseismic data. Despite the strong tendency of the hydraulic fracture to propagate east toward the drift, driven by the thermal stress gradient surrounding the drift, the eastwards growth in all the stimulation episodes was halted by OT-P Connector. According to classic 2D intersection models (Gu et al., 2012; Renshaw & Pollard, 1995), a hydraulic fracture could cross (including crossing with a lateral offset), or be arrested by a natural fracture depending on a number of geometrical, geomechanical, and hydraulic factors. At the EGS Collab Experiment 1 testbed, OT-P Connector is under much greater compressive stress than is the hydraulic fracture, and the two fractures are nearly perpendicular to each other. These two factors favor a “crossing” mode. However, high hydraulic conductivity of OT-P Connector and the relatively mild stimulation rate might have resulted in the observed temporary hydraulic “arrest.” Only the two stimulation episodes with relatively long durations, 525B and 625P, were able to propagate fractures to the east of OT-P Connector. The temporary arrest in other episodes is evident in Figure 3: As seen in Figure 3c, during stimulation 524 the fracture arrived at OT-P Connector at 22:40, but the next 12 min of stimulation did not cause significant microseismic events on the other side the natural fracture. The same took place in stimulation 525A as shown in Figure 3d. Fractures on the east side of OT-P Connector only developed during stimulations 525B and 625I, both of which were much longer than stimulations 524 and 525B. East-side fracturing, signified by orange-colored dots in Figure 3e and dark purple dots in Figure 3h, started after 20 min of stimulation while in all relevant stimulations, fracture fronts reached OT-P Connector in ~10 min.

The partial-arrest-partial-cross behavior observed across OT-P Connector is likely caused by the highly heterogeneous aperture distribution along this natural fracture, as can be inferred from the core photos in Figure 1. Even though this fracture is known to have wide aperture, such wide, open aperture cannot exist throughout the entire fracture area as the fracture needs to bear the great in-situ stress through wall-to-wall

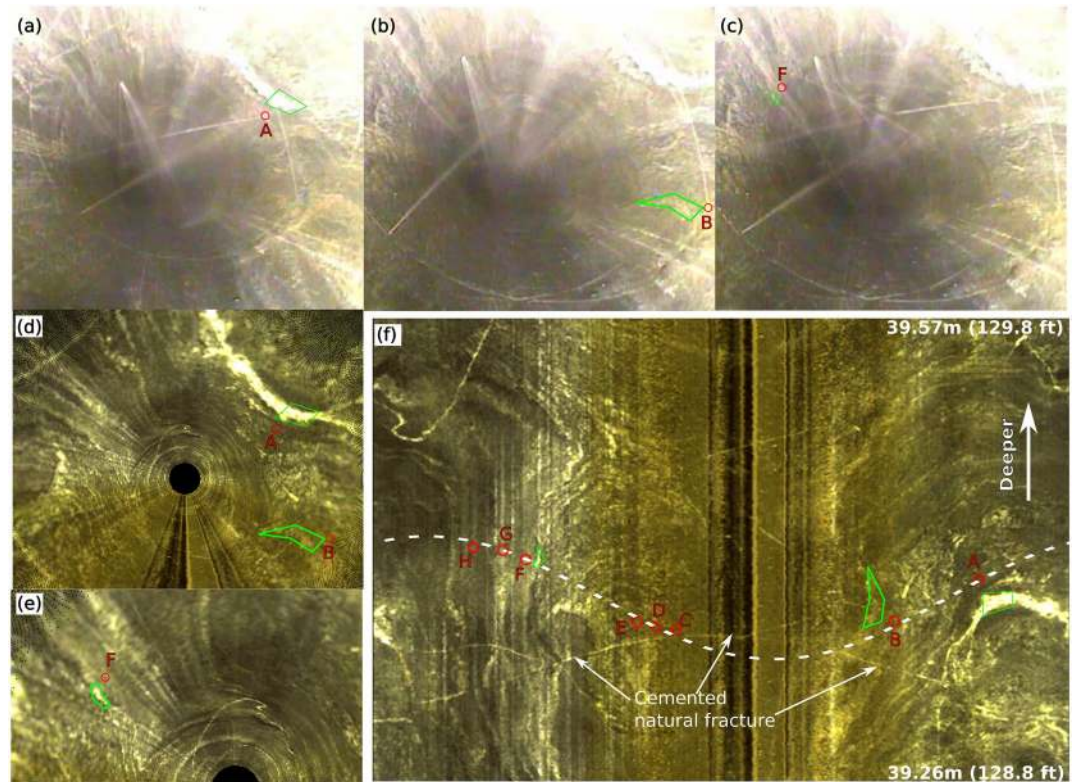


Figure 7. The method to accurately locate the jets. (a) to (c) are three frames in the downhole camera video. (d) and (e) are simulated downhole camera image from well E1-P's televiwer log. (f) is unwrapped televiwer log covering the concerned segments. Three jets, A, B, and F, are located in this illustration. Enclosed by green polygons are the wellbore features used to anchor the jet locations. The white dashed curve in (f) is the trace of the fitted plane through the eight jets. The anchoring of other jet locations was performed in a similar fashion.

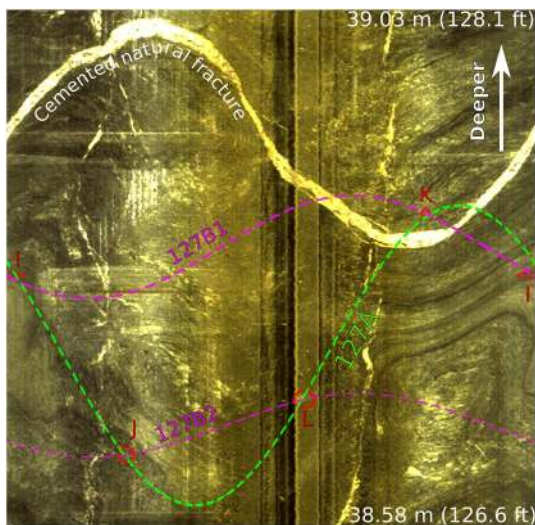


Figure 8. Locations of the jets in the cluster near 38.8-m (127 ft) depth in well E1-P. The green dashed line is the trace of a plane that could cut through all the four jets in this segment. The two magenta curves correspond to two planes aligning with jets I-K, and jets J-L, respectively.

contact. Therefore, the fracture has to be partially closed. As fractures W-S and W-N each intersect OT-P Connector over a long intersection line, the segment that hits the open part of OT-P Connector is likely to be arrested while the segment hitting the closed/sealed part is more likely to cross. This hypothesis was supported by observations during two long-term low-rate circulation tests that took place in October to November 2018, and March 2019 to March 2020, respectively. In both tests, the 50-m (164 ft) notch was subjected to continuous injection at 400 ml/min. Flow into well E1-P was observed at its intersection with OT-P Connector and at the jetting locations. Flow from OT-P Connector into E1-P must have originated from fluid fed into OT-P Connector from W-N and/or W-S at the “arrest” locations; flow from the jetting locations must have crossed OT-P Connector.

The microseismic data indicate reorientation of the hydraulic fractures after crossing the natural fracture. The spatial configuration of the four large fractures suggests that fracture E-N is the continuation of fracture W-N with a rotation of the fracture plane; E-S is the continuation of W-S with a rotation of the fracture plane. The fracture planes' reorientation suggests OT-P Connector marks a discontinuity in the in-situ stress and/or in the rock's fabric orientation. This argument seems to be supported by a replot of Figure 3 that separates fractures to the west and east of OT-P Connector. The figure is included as Supporting Information Figure S1.

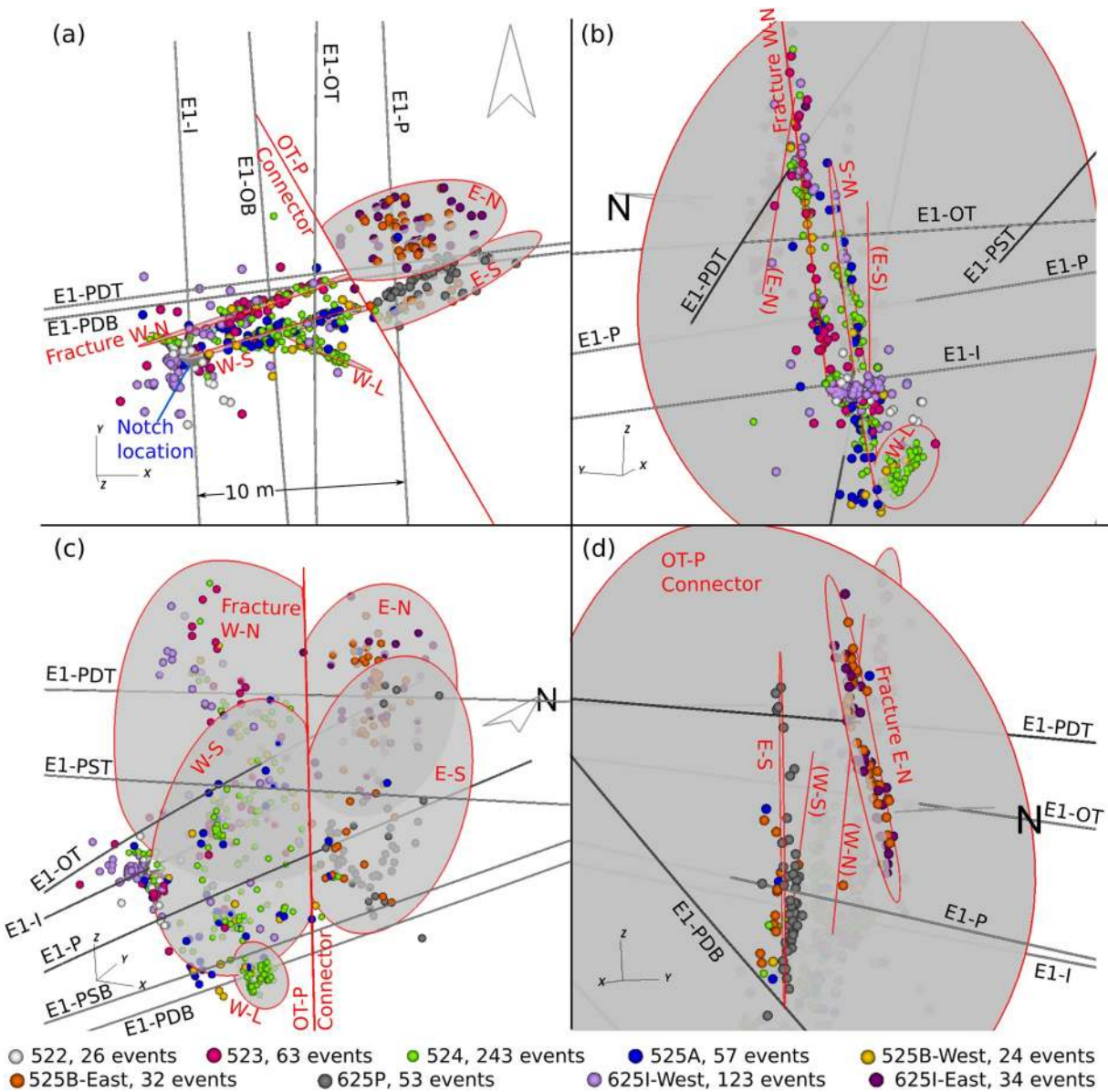


Figure 9. The distribution of microseismic source locations associated with the seven stimulation episodes. Colors of the locations differentiate the stimulation episodes and whether the locations are to the east or west of OT-P Connector. Four view angles are used in the subfigures: (a) viewing from top along OT-P Connector and two fitted hydraulic fracture planes west of OT-P Connector; (b) viewing from west, along the fitted main hydraulic fracture planes; (c) viewing from south-southeast, horizontally along OT-P Connector; and (d) viewing from east, approximately parallel to the two planar features to the east of OT-P Connector. Perimeters of fitted fractures and names of the fractures are in red color. In (b) and (d), the intersections of the two fractures on the other side of OT-P Connector with the natural fracture are also shown as red line segments. An animated version of this figure is included in the Supporting Information.

The two sets of three-way intersections between the fractures: W-N/OT-P Connector/E-N and W-S/OT-P Connector/E-S are depicted in Figures 9 and 10 in simplistic ways. The actual geometrical and topological relationships around these intersections can be very complicated. This is inferred from the complex jetting patterns between 38-m and 40-m deep in E1-P. Although the deeper jetting cluster coincides with the idealized intersection point between E1-P and fracture E-S and the jet origins seem to form a plane, this plane's orientation is different from that of E-S. Recall that the deeper jetting cluster conformed to a plane striking 108.4° and dipping 52.9° as constrained in Figure 7, whereas fracture E-S strikes 60° and dips 88° . Considering the even more complex pattern in the shallower jetting cluster, we acknowledge that fracture flow near this three-way intersection region must be very complex, might involve flowing through some natural fractures, and cannot be fully constrained using the existing data.

Table 3
Linear-Regression Results for the Five Fracture Planes

Fracture	Num. of events	Function	R^2	Strike (°)	Dip (°)
W-N	112	$y = 0.324x + 0.168z - 1576.5$	0.867	72	81
W-S	147	$y = 0.238x + 0.198z - 1510.9$	0.858	77	79
W-L	62	$y = -0.435x + 0.067z - 948.8$	0.761	113	86
E-N	82	$y = 0.397x - 0.142z - 1599.7$	0.587	248	82
E-S	80	$y = 0.581x + 0.047z - 1775.8$	0.662	60	88

5.5. The Role of Natural Fractures: Cemented (Mineral-Filled) Fractures

As described in Section 2.2, the EGS Collab testbed contains an extensive network of natural fractures including both open and cemented fractures. An order-of-magnitude estimation of the trace length along the intersections between the hydraulic fractures and the natural fractures can be obtained by estimating the “fracture intensity” (Dershowitz & Einstein, 1988) in terms of trace length per unit surface area, or equivalently intersection counts per unit wellbore length. The 206 fracture intersections along the eight wellbores with a total length of 466.7 m indicate an approximate fracture intensity of 0.4 m² of fracture area per unit m³ of rock body, or 0.4 m of trace length per unit m² of fracture area. The total area of the four main hydraulic fractures is estimated to be larger than

400 m², so the total trace length of the intersections between the hydraulic fractures and natural fractures in the testbed is roughly 160 m, indicating intensive hydraulic-natural fracture intersections in this relatively small testbed.

Among the five delineated planar fractures from microseismic events, fracture W-L (west of OT-P Connector, lower in the testbed) is, based on its orientation and location, less likely a hydraulic fracture than are the other four. As no well intersects fracture W-L, there was no direct indication of the nature of this fracture. However, some less definitive evidence exists. At 44.2-m deep in well E1-OT, a vein 10-cm thick was visible in the core and also in this well’s televiewer log. The vein (orientation depicted by an orange disk with dashed perimeter in Figure 12c) appears to be approximately coplanar with fracture W-L as shown in Figure 12c. This could suggest that the observed microseismic events around W-L were caused by the opening or slipping of the interface between the vein and the country rock as pressurized water was fed into the interface from fracture W-S. This evidence is relatively weak as well E1-OT is ~10 m above fracture W-L and this vein is not clearly seen in other wells. Figure 11 shows that most of the microseismic events on W-L were between 22:40 and 22:50 (UTC) in stimulation 524 (May 24, 2018). Although three later stimulation episodes, 525A, 525B, and 625I were longer and pumped larger volumes of fluid, few additional microseismic events were generated on W-L. Therefore, the area of the activated natural fracture, at least the area that generated observable microseismic signals, is very limited and did not tend to grow even under sustained pressurization.

Cemented natural fractures are also visible near the two jetting clusters in well E1-P, at ~38.8-m (127 ft) and 39.4-m (129 ft) deep, respectively. Traces of the natural fractures, as marked in Figures 7 and 8, clearly

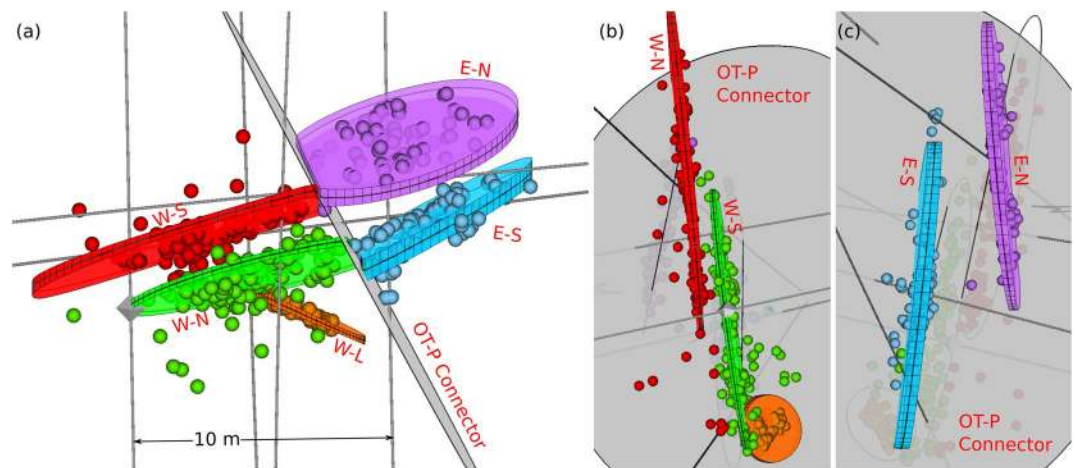


Figure 10. 95% confidence interval of the five fitted fracture planes visualized as semitransparent “disks.” The three subfigures are views from different angles. The fracture plane intervals and the associated microseismic source locations are given the same colors. Source locations near well E1-I are not shown.

Table 4 Intersections Between Fitted Fracture Planes and Wellbores			
Fracture	Well	Depth in well (m)	Notes
W-N	E1-I	51.3	No apparent feature; no apparent difference between prestimulation and poststimulation based on acoustic log
W-N	E1-OT	46.4	Strong temperature anomaly at 46 m in stimulation 524; weaker temperature anomalies at 46 m in stimulations 523, 525A, and 525B
W-S	E1-I	50.2	Precut notch at 50.2 m for initiating fracture
W-S	E1-OT	45.0	Strong temperature anomaly at 44.5 m in stimulations 524, 525A, 525B, and 625I
E-S	E1-P	39.6	One jetting cluster at 39.4 m observed in stimulation 525B. The injection interval pressurized in stimulation 625P was between 39.3 and 40.6 m
E-S	E1-PDB	32.3	Temperature anomaly at 32.3 m in stimulation 625P

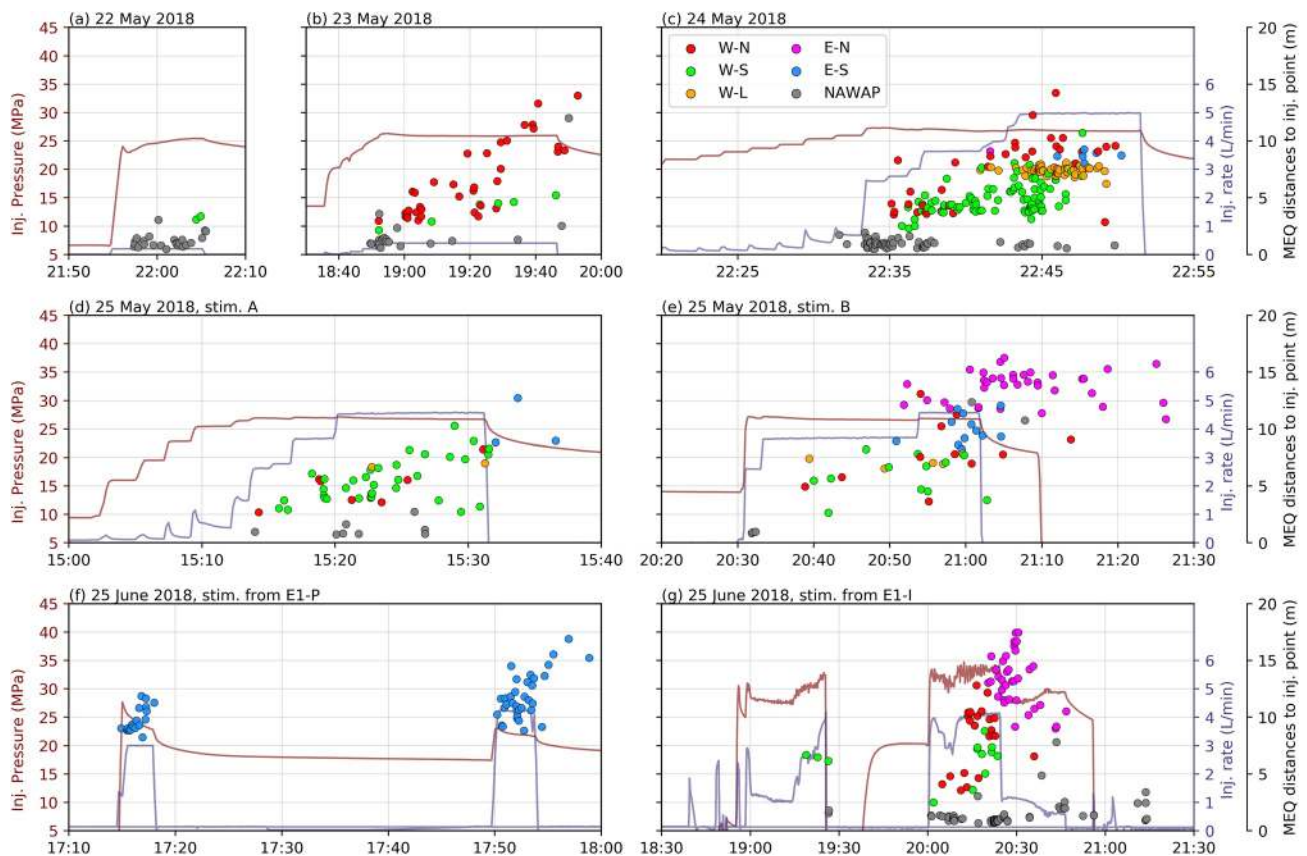


Figure 11. Injection history and the associated microseismic events revisualized based on Figure 3. The microseismic events are colored based on the identified fracture planes that are apparently associated with. The color mapping is the same as that in Figures 9 and 12. In the legend, NAWAP means “not associated with any plane”.

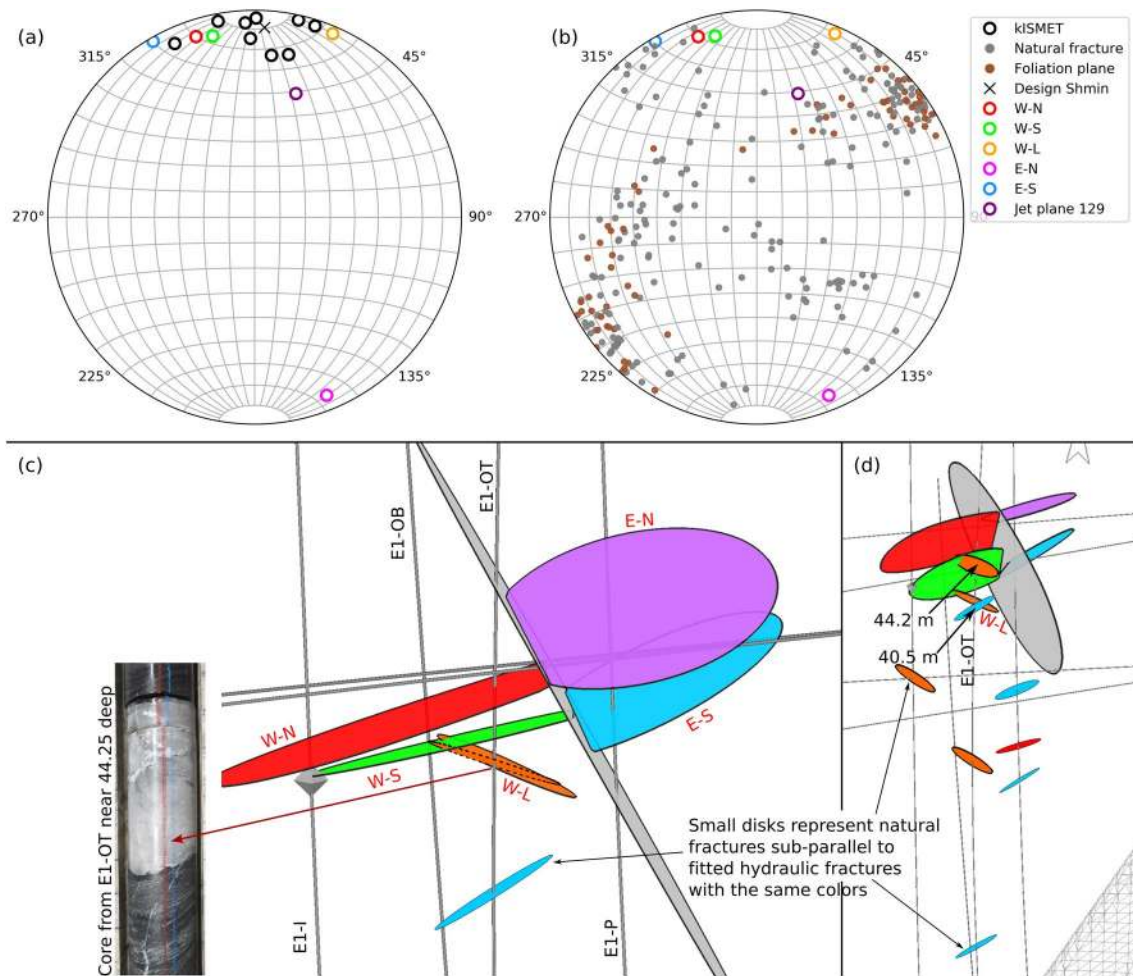


Figure 12. The relationship among the five postulated hydraulic fracture planes, the jetting plane delineated in Figure 7, natural fractures in the test bed, and hydraulic fracture planes logged in the KISMET experiment. (a) Lower hemisphere pole plot of the hydraulic fracture planes and the jetting plane in comparison with the 10 KISMET hydraulic fractures. The orientation of S_{hmin} based on KISMET results is also shown. (b) Comparison with all the natural fractures and logged foliation planes in the testbed in a pole plot. (d) and (e) show the relationship between the five hydraulic fracture planes (large colored planes) and natural fractures (small disks) that are subparallel (within 10°) to any of the fitted hydraulic fracture planes. The natural fractures are colored the same as the fitted hydraulic fractures that they are subparallel to.

intersect the inferred traces of the hydraulic fractures, indicating that these cemented natural fractures intersected the hydraulic fractures near the well. However, no influence of the natural fractures on the trajectories of the hydraulic fractures, either mechanical or hydraulic, is evident. This means these cemented natural fractures behaved as a part of the rock continuum during the propagation of the hydraulic fracture. This notion is directly supported by laboratory testing (Frash et al., 2019a, 2019b; Ye et al., 2019, 2020) of rock samples cut from cores retrieved from the Collab Experiment 1 testbed. Those experiments found that cemented fractures or veins are stronger than the phyllite rock along the foliation plane direction.

The relatively long, low-rate injection in June 2018, as shown in Figure 3f offers additional insight into the behavior of natural fractures in this testbed. The injection that started on June 20 lasted >30 h. Although the flow rate was mostly as low as 40 ml/min, the injection pressure showed clear pressure-limiting behavior with a value similar to that from the high-rate injections. Therefore, the hydraulic fracture was jacked open during this injection, and the same fluid pressure as that in the stimulation episodes existed along the hydraulic fractures to drive pressure diffusion into the natural fractures intersecting the hydraulic fracture. The fact that no microseismic events were observed during this prolonged injection indicate that either the pressure diffusion into the natural fracture was very minimal or that this process was “aseismic.” This observation strengthens the conclusion that most of the microseismic events recorded were due to opening-mode

fracture propagation. However, the scarcity of microseismic events from shearing of natural fractures in these experiments should not be generalized beyond the specific conditions in these experiments: relatively small spatial scale and low injection rate. In fact, the signal from these microseismic events was weak, making it challenging to quantify their magnitudes or focal mechanisms. Had the conditions enabled the generation of stronger shearing events, these weak tensile events could have been overshadowed.

6. Conclusions

We presented a comprehensive set of data acquired during the first suite of hydraulic stimulation experiments performed between May and June 2018 at the EGS Collab testbed on the 4,850 ft (1.48 km) level of SURF. From very high-quality microseismic data, we discerned five distinct planar features. Incorporating additional evidence including prior mini-frac results in a nearby location, distributions of natural fractures in the testbed, distributed temperature measurements along boreholes, and directly observed intersections between fractures and wellbores, we conclude with high certainty that four of the planar features are new hydraulic fractures created by the stimulations and the other one more likely represents a segment of a natural fracture activated through either shearing or opening. This provides rare evidence to support the notion that tensile-mode hydraulic fractures could generate microseismic signals.

The data revealed that two hydraulic fractures initiated from the isolated injection section and propagated in a largely parallel fashion, 1.5 m apart, until they intersected a major natural fracture dubbed the OT-P Connector. Complex interactions between the hydraulic fractures and the natural fracture were evident. Likely due to the high spatial variability of the natural fracture, part of the hydraulic fractures' front was arrested or deterred by OT-P Connector whereas part of it crossed the natural fracture, emerging as two hydraulic fractures on the other side of OT-P Connector. The crossing was accompanied by a minor rotation of the fracture planes, indicating that the natural fracture marks discontinuities in in-situ stress or rock fabric.

Despite the large number of cemented, mineral-filled natural fractures present in the testbed, there is little indication of interference between them and the hydraulic fractures. The fifth planar feature (denoted fracture W-L in this work) discerned from the microseismic events, relatively small in size, could have been the result of tensile and/or shearing activation of a natural fracture through its intersection with one of the hydraulic fractures. It appears to be coplanar with a vein visible from one of the wells, but veins at this testbed tend to be highly variable and discontinuous. Therefore, this attribution is not supported by strong evidence. Direct observations from well E1-P, where intersections between cemented fractures and hydraulic fractures were directly observed, show that most cemented natural fractures tend to behave as a part of the rock continuum, which is also supported by available laboratory rock mechanic tests. It should be emphasized that great caution must be taken when extrapolating conclusions from an intermediate-scale testbed to a full-scale scenario. The presence of a singularly prominent natural fracture and the low pumping rate might have prevented the majority of the natural fractures from exercising observable influence on response of the rock-fracture-fluid system.

Thanks to the comprehensive monitoring system at the testbed and the opportunity to make various direct observations, many of the above conclusions were attained with a great certainty, testifying the benefits of the intermediate-scale testbed for subsurface research.

Appendix A

The EGS Collab Team includes J. Ajo-Franklin, T. Baumgartner, K. Beckers, D. Blankenship, A. Bonneville, L. Boyd, S. Brown, J.A. Burghardt, C. Chai, T. Chen, Y. Chen, K. Condon, P.J. Cook, D. Crandall, P.F. Dobson, T. Doe, C.A. Doughty, D. Elsworth, J. Feldman, A. Foris, L.P. Frash, Z. Frone, P. Fu, K. Gao, A. Ghassemi, Y. Guglielmi, B. Haimson, A. Hawkins, J. Heise, M. Horn, R.N. Horne, J. Horner, M. Hu, H. Huang, L. Huang, K.J. Im, M. Ingraham, R.S. Jayne, T.C. Johnson, B. Johnston, S. Karra, K. Kim, D.K. King, T. Kneafsey, H. Knox, J. Knox, D. Kumar, K. Kutun, M. Lee, K. Li, Z. Li, M. Maceira, P. Mackey, N. Makedonska, C.J. Marone, E. Mattson, M.W. McClure, J. McLennan, T. McLing, C. Medler, R.J. Mellors, E. Metcalfe, J. Miskimins, J. Moore, J.P. Morris, S. Nakagawa, G. Neupane, G. Newman, A. Nieto, C.M. Oldenburg, W. Pan, T. Paronish, R. Pawar, P. Petrov, B. Pietzyk, R. Podgorney, Y. Polsky, J. Pope, S. Porse, B.Q. Roberts, M. Robertson,

W. Roggenthen, J. Rutqvist, D. Rynders, M. Schoenball, P. Schwering, V. Sesetty, A. Singh, M.M. Smith, H. Sone, F.A. Soom, P. Sprinkle, C.E. Strickland, J. Su, D. Templeton, J.N. Thomle, C. Ulrich, N. Uzunlar, A. Vachaparampil, C.A. Valladao, W. Vandermeer, G. Vandine, D. Vardiman, V.R. Vermeul, H.F. Wang, J. Weers, N. Welch, M.D. White, P. Winterfeld, T. Wood, S. Workman, H. Wu, Y.S. Wu, E.C. Yildirim, Y. Zhang, Y.Q. Zhang, Q. Zhou, M.D. Zoback, led by T. Kneafsey and D. Blankenship.

Data Availability Statement

Injection rates and injection pressure for all the stimulations mentioned in the current paper are available at Geothermal Data Repository (GDR) through submission <http://gdr.openei.org/submissions/1229>. Full downhole camera survey footage during stimulation 525B is available at <https://gdr.openei.org/submissions/1227>. The supplementary data include the microseismic catalog, the geometries of the wellbores and delineated fractures, DTS data, GIF animations of the model including the microseismic cloud, as well as selected footages of the downhole camera survey.

Acknowledgments

This material was based upon work supported by the U.S. Department of Energy, Office of Energy Efficiency and Renewable Energy (EERE), Office of Technology Development, Geothermal Technologies Office, under Award Number DE-AC52-07NA27344 with LLNL, Award Number DE-AC05-76RL01830 with PNNL, Award Number DE-AC02-05CH11231 with LBNL, and contract number DE-NA0003525 with Sandia National Laboratories, etc. Publication release for this manuscript is under LLNL-JOUR-811416. The United States Government retains, and the publisher, by accepting the article for publication, acknowledges that the United States Government retains a nonexclusive, paid-up, irrevocable, world-wide license to publish or reproduce the published form of this manuscript, or allow others to do so, for United States Government purposes. We thank the drillers of Agapito Associates, Inc., for their skill and dedicated efforts to create our testbed boreholes. The research supporting this work took place in whole or in part at the Sanford Underground Research Facility in Lead, South Dakota. The assistance of the Sanford Underground Research Facility and its personnel in providing physical access and general logistical and technical support is acknowledged. DOE provides public access to these results of federally sponsored research in accordance with the DOE Public Access Plan (<http://energy.gov/downloads/doe-public-access-plan>).

References

Ajo-Franklin, J., Daley, T., Butler-Veytia, B., Peterson, J., Wu, Y., Kelly, B., & Hubbard, S. (2011). Multi-level continuous active source seismic monitoring (ML-CASSM): Mapping shallow hydrofracture evolution at a TCE contaminated site. In *2011 SEG Annual Meeting, Society of Exploration Geophysicists* (pp. 3727–3731). <https://doi.org/10.1190/1.3627980>

Bonnet, E., Bour, O., Odling, N. E., Davy, P., Main, I., Cowie, P., & Berkowitz, B. (2001). Scaling of fracture systems in geological media. *Reviews of Geophysics*, 39(3), 347–383. <https://doi.org/10.1029/1999RG000074>

Brown, D. W., Duchane, D. V., Heiken, G., & Hrisco, V. T. (2012). *Mining the earth's heat: Hot dry rock geothermal energy*. Berlin: Springer.

Caddey, S. W., Bachman, R. L., Campbell, T. J., Reid, R. R., & Otto, R. P. (1991). The Homestake Gold Mine, an Early Proterozoic iron-formation-hosted gold deposit, Lawrence County, South Dakota (U.S. Geological Survey Bulletin 1857-J, pp. 67). *Geology and Resources of Gold in the United States*. <https://doi.org/10.3133/b1857J>

Ciezobka, J., Courtier, J., & Wicker, J. (2018). Hydraulic fracturing test site (HFTS)—Project Overview and summary of results. *Paper presented at Proceedings of the 6th Unconventional Resources Technology Conference*. <https://doi.org/10.15530/URTEC-2018-2937168>

Daley, T. M., Ajo-Franklin, J. B., & Doughty, C. (2011). Constraining the reservoir model of an injected CO₂ plume with crosswell CASSM at the Frio-II brine pilot. *International Journal of Greenhouse Gas Control*, 5(4), 1022–1030. <https://doi.org/10.1016/j.ijggc.2011.03.002>

Daley, T. M., Solbau, R. D., Ajo-Franklin, J. B., & Benson, S. M. (2007). Continuous active-source seismic monitoring of CO₂ injection in a brine aquifer. *Geophysics*, 72(5), A57–A61. <https://doi.org/10.1190/1.2754716>

Dershowitz, W. S., & Einstein, H. H. (1988). Characterizing rock joint geometry with joint system models. *Rock Mechanics and Rock Engineering*, 21(1), 21–51. <https://doi.org/10.1007/BF01019674>

Dutler, N., Valley, B., Gischig, V., Villiger, L., Krietsch, H., Doetsch, J., et al. (2019). Hydraulic fracture propagation in a heterogeneous stress field in a crystalline rock mass. *Solid Earth*, 10(6), 1877–1904. <https://doi.org/10.5194/se-10-1877-2019>

Engelder, T., Lash, G. G., & Uzcátegui, R. S. (2009). Joint sets that enhance production from middle and upper Devonian gas shales of the Appalachian basin. *American Association of Petroleum Geologists Bulletin*, 93(7), 857–889. <https://doi.org/10.1306/03230908032>

Fisher, M. K., & Warpinski, N. R. (2012). Hydraulic-fracture-height growth: Real data. *SPE Production & Operations*, 27(1), 8–19. <https://doi.org/10.2118/145949-PA>

Frash, L. P., Carey, J. W., Welch, N. J., & EGS Collab Team. (2019a). EGS Collab Experiment 1 geomechanical and hydrological properties by triaxial direct shear. *Paper presented at Proceedings of the 44th Workshop on Geothermal Reservoir Engineering, February 11–13, 2019*.

Frash, L. P., Welch, N. J., Carey, J. W., & EGS Collab Team. (2019b). Geomechanical evaluation of natural shear fractures in the EGS collab experiment 1 test bed. *Paper presented at Proceedings of the 53rd US Rock Mechanics/Geomechanics Symposium, June 23–26, 2019*.

Fu, P., Huang, J., Settgest, R. R., Morris, J. P., & Ryerson, F. J. (2019). Apparent toughness anisotropy induced by roughness of in-situ stress: A mechanism that hinders vertical growth of hydraulic fractures and its simplified modeling. *SPE Journal*, 24(5), 2148–2162. <https://doi.org/10.2118/194359-PA>

Fu, P., Johnson, S. M., & Carrigan, C. R. (2013). An explicitly coupled hydro-geomechanical model for simulating hydraulic fracturing in arbitrary discrete fracture networks. *International Journal for Numerical and Analytical Methods in Geomechanics*, 37(14), 2278–2300. <https://doi.org/10.1002/nag.2135>

Fu, P., White, M. D., Morris, J. P., Kneafsey, T. J., & EGS Collab Team. (2018). Predicting hydraulic fracture trajectory under the influence of a mine drift in EGS collab experiment I. *Paper presented at Proceedings of the 43rd Workshop on Geothermal Reservoir Engineering, Stanford University, Stanford, California, February 12–14, 2018*.

Gale, J. F. W., Elliott, S. J., & Laubach, S. E. (2018). Hydraulic fractures in core from stimulated reservoirs: Core fracture description of HFTS slant core, Midland Basin, West Texas. *Paper presented at Proceedings of the 6th Unconventional Resources Technology Conference*. <https://doi.org/10.15530/urtec-2018-2902624>

Gale, J. F. W., Elliott, S. J., Li, J. Z., & Laubach, S. E. (2019). Natural fracture characterization in the Wolfcamp formation at the hydraulic fracture test site (HFTS), Midland Basin, Texas. *Paper presented at Proceedings of the 7th Unconventional Resources Technology Conference*. <https://doi.org/10.15530/urtec-2019-644>

Gale, J. F. W., Laubach, S. E., Olson, J. E., Eichhubl, P., & Fall, A. (2017). Natural fractures in shale: A review and new observations. *American Association of Petroleum Geologists Bulletin*, 101(8), 2165–2216. <https://doi.org/10.1306/08121413151>

Gale, J. F. W., Reed, R. M., & Holder, J. (2007). Natural fractures in the Barnett Shale and their importance for hydraulic fracture treatments. *American Association of Petroleum Geologists Bulletin*, 91(4), 603–622. <https://doi.org/10.1306/11010606061>

Genter, A., Evans, K., Cuenot, N., Fritsch, D., & Sanjuan, B. (2010). Contribution of the exploration of deep crystalline fractured reservoir of Soultz to the knowledge of enhanced geothermal systems (EGS). *Comptes Rendus Geoscience*, 342(7–8), 502–516. <https://doi.org/10.1016/j.crte.2010.01.006>

- Gu, H., Weng, X., Lund, J., MacK, M., Ganguly, U., & Suarez-Rivera, R. (2012). Hydraulic fracture crossing natural fracture at nonorthogonal angles: A criterion and its validation. *SPE Production and Operations*, 27(1), 20–26. <https://doi.org/10.2118/139984-PA>
- Guglielmi, Y., Cappa, F., Lançon, H., Janowczyk, J. B., Rutqvist, J., Tsang, C. F., & Wang, J. S. Y. (2014). ISRM suggested method for step-rate injection method for fracture in-situ properties (SIMFIP): Using a 3-components borehole deformation sensor. *Rock Mechanics and Rock Engineering*, 47(1), 303–311. <https://doi.org/10.1007/s00603-013-0517-1>
- Hausner, M. B., Suárez, F., Glander, K. E., Giesen, N. V. D., Selker, J. S., & Tyler, S. W. (2011). Calibrating single-ended fiber-optic Raman spectra distributed temperature sensing data. *Sensors*, 11(11), 10859–10879. <https://doi.org/10.3390/s111110859>
- Heise, J. (2015). The Sanford underground research facility at Homestake. *Journal of Physics: Conference Series*, 606(1), 12015. <https://doi.org/10.1088/1742-6596/606/1/012015>
- Hubbert, K. M., & Willis, D. G. (1957). Mechanics of hydraulic fracturing. *Transactions of the American Institute of Mining and Metallurgical Engineers*, 210(6), 153–163. <https://doi.org/10.2118/686-g>
- Jeffrey, R. G., Bunger, A., LeCampion, B., Zhang, X., Chen, Z., van As, A., et al. (2009). Measuring hydraulic fracture growth in naturally fractured rock. In *SPE Annual Technical Conference and Exhibition* (Vol. 6, pp. 3750–3768). Society of Petroleum Engineers. <https://doi.org/10.2118/124919-MS>
- Johnson, T. C., Slater, L. D., Ntarlagiannis, D., Day-Lewis, F. D., & Elwaseif, M. (2012). Monitoring groundwater-surface water interaction using time-series and time-frequency analysis of transient three-dimensional electrical resistivity changes. *Water Resources Research*, 48, W07506. <https://doi.org/10.1029/2012WR011893>
- Kneafsey, T. J., Blankenship, D., Dobson, P. F., Morris, J. P., White, M. D., Fu, P., et al. (2020). The EGS Collab project: Learning from experiment 1. *Paper presented at Proceedings of the 45th Workshop on Geothermal Reservoir Engineering, Stanford University, Stanford, California, February 10–12, 2020*.
- Krietsch, H., Doetsch, J., Dutler, N., Jalali, M., Gischig, V., Loew, S., & Amann, F. (2018). Comprehensive geological dataset describing a crystalline rock mass for hydraulic stimulation experiments. *Scientific Data*, 5, 180269. <https://doi.org/10.1038/sdata.2018.269>
- Krietsch, H., Gischig, V., Evans, K., Doetsch, J., Dutler, N. O., Valley, B., & Amann, F. (2019). Stress measurements for an in situ stimulation experiment in crystalline rock: Integration of induced seismicity, stress relief and hydraulic methods. *Rock Mechanics and Rock Engineering*, 52(2), 517–542. <https://doi.org/10.1007/s00603-018-1597-8>
- Maxwell, S. C., Rutledge, J., Jones, R., & Fehler, M. (2010). Petroleum reservoir characterization using downhole microseismic monitoring. *Geophysics*, 75(5), 75A129–75A137. <https://doi.org/10.1190/1.3477966>
- McClure, M. W., & Horne, R. N. (2014). An investigation of stimulation mechanisms in Enhanced Geothermal Systems. *International Journal of Rock Mechanics and Mining Sciences*, 72, 242–260. <https://doi.org/10.1016/j.ijrmm.2014.07.011>
- McClure, M. W., Mohsen, B., Sogo, S., & Jian, H. (2016). Fully coupled hydromechanical simulation of hydraulic fracturing in 3D discrete-fracture networks. *SPE Journal*, 21(4), 1302–1320. <https://doi.org/10.2118/173354-ms>
- Oldenburg, C. M., Dobson, P. F., Wu, Y., Cook, P. J., Kneafsey, T. J., Nakagawa, S., et al. (2016). *Intermediate-scale hydraulic fracturing in a deep mine, kISMET project summary 2016, LBNL-1006444*. Berkeley, CA: Lawrence Berkeley National Laboratory. <https://doi.org/10.2172/1338937>
- Raterman, K. T., Farrell, H. E., Mora, O. S., Janssen, A. L., Gomez, G. A., Busetti, S., et al. (2018). Sampling a stimulated rock volume: An Eagle Ford example. *SPE Reservoir Evaluation and Engineering*, 21(4), 927–941. <https://doi.org/10.2118/191375-PA>
- Renshaw, C., & Pollard, D. (1995). An experimentally verified criterion for propagation across unbounded frictional interfaces in brittle, linear elastic materials. *International Journal of Rock Mechanics and Mining Science & Geomechanics Abstracts*, 32(3), 237–249. [https://doi.org/10.1016/0148-9062\(94\)00037-4](https://doi.org/10.1016/0148-9062(94)00037-4)
- Riffault, J., Dempsey, D., Karra, S., & Archer, R. (2018). Microseismicity cloud can be substantially larger than the associated stimulated fracture volume: The case of the Paralana enhanced geothermal system. *Journal of Geophysical Research: Solid Earth*, 123, 6845–6870. <https://doi.org/10.1029/2017JB015299>
- Schoenball, M., Ajo-Franklin, J. B., Blankenship, D., Chai, C., Dobson, P. F., Kneafsey, T. J., et al. (2020). Creation of a mixed-mode fracture network at meso-scale through hydraulic fracturing and shear stimulation. *Journal of Geophysical Research: Solid Earth*, 125, e2020JB019807. <https://doi.org/10.1029/2020JB019807>
- Schwering, P. C., Doe, T. W., Roggenthen, W. M., Neupane, G. H., Johnston, H., Dobson, P. F., & The EGS Collab Team. (2020). Deterministic discrete fracture network (DFN) model for the EGS Collab project on the 4850 level of the Sanford Underground Research Facility (SURF). *Paper presented at the 54th U.S. Rock Mechanics/Geomechanics Symposium, Physical Event Cancelled, June 2020 (Paper No. ARMA 20-1900)*.
- Settgast, R. R., Fu, P., Walsh, S. D. C., White, J. A., Annavarapu, C., & Ryerson, F. J. (2017). A fully coupled method for massively parallel simulation of hydraulically driven fractures in 3-dimensions. *International Journal for Numerical and Analytical Methods in Geomechanics*, 41(5), 627–653. <https://doi.org/10.1002/nag.2557>
- Shapiro, S. A., & Dinske, C. (2009). Fluid-induced seismicity: Pressure diffusion and hydraulic fracturing. *Geophysical Prospecting*, 57(2), 301–310. <https://doi.org/10.1111/j.1365-2478.2008.00770.x>
- Shapiro, S. A., Dinske, C., & Rother, E. (2006). Hydraulic-fracturing controlled dynamics of microseismic clouds. *Geophysical Research Letters*, 33, L14312. <https://doi.org/10.1029/2006GL026365>
- Sherman, C. S., Morris, J. P., Fu, P., & Settgast, R. R. (2019). Recovering the microseismic response from a geomechanical simulation. *Geophysics*, 84(4), KS133–KS142. <https://doi.org/10.1190/geo2018-0184.1>
- Ugueto, G., Huckabee, P., Wojtaszek, M., Daredia, T., & Reynolds, A. (2019). New near-wellbore insights from fiber optics and downhole pressure gauge data. In *SPE hydraulic fracturing technology conference and exhibition*. Society of Petroleum Engineers. <https://doi.org/10.2118/194371-MS>
- US Department of Energy. (2019). *GeoVision: Harnessing the heat beneath our feet* (DOE/EE-1306). Retrieved from <https://www.energy.gov/eere/geothermal/geovision>
- Wang, H. F., Lee, M. Y., Doe, T. W., Haimson, B. C., Oldenburg, C. M., & Dobson, P. F. (2017). In situ stress measurement at 1550-meters depth at the kISMET test site in Lead, S.D. In *51st U.S. Rock Mechanics/Geomechanics Symposium, San Francisco, CA, June 25–28, 2017 (Paper No. ARMA 17-651, p. 7)*.
- Warpinski, N. R., Lorenz, J. C., Branagan, P. T., Myal, F. R., & Gall, B. L. (1993). Examination of a cored hydraulic fracture in a deep gas well. *SPE Production and Facilities*, 8(3), 150–158. <https://doi.org/10.2118/22876-PA>
- Warpinski, N. R., Mayerhofer, M. J., Vincent, M. C., Cipolla, C. L., & Lolon, E. P. (2009). Stimulating unconventional reservoirs: Maximizing network growth while optimizing fracture conductivity. *Journal of Canadian Petroleum Technology*, 48(10), 39–51. <https://doi.org/10.2118/114173-pa>

- Weng, X., Kresse, O., Cohen, C.-E., Wu, R., & Gu, H. (2011). Modeling of hydraulic-fracture-network propagation in a naturally fractured formation. *SPE Production and Operations*, 26(4), 368–380. <https://doi.org/10.2118/140253-PA>
- Willis-Richards, J., Watanabe, K., & Takahashi, H. (1996). Progress toward a stochastic rock mechanics model of engineered geothermal systems. *Journal of Geophysical Research*, 101(B8), 17481–17496. <https://doi.org/10.1029/96JB00882>
- Wu, H., Fu, P., Morris, J. P., Mattson, E. D., Neupane, G., Hawkins, A., et al. (2021). Characterization of flow and transport in a fracture network at the EGS Collab field experiment through stochastic modeling of tracer recovery. *Journal of Hydrology*, 593, 125888. <https://doi.org/10.1016/j.jhydrol.2020.125888>
- Ye, Z., Ghassemi, A., & Kneafsey, T. (2020). Deformation, failure and permeability evolution of sealed fractures in EGS collab Poorman schist. Paper presented at *Proceedings of the 45th Workshop on Geothermal Reservoir Engineering, Stanford University, Stanford, California, February 10–12, 2020*.
- Ye, Z., Vachaparampil, A., Zhou, X., Ghassemi, A., & Kneafsey, T. (2019). Failure behavior of the Poorman schist and its fractures from EGS collab stimulation site. Paper presented at *Proceedings of the 44th Workshop on Geothermal Reservoir Engineering, Stanford University, Stanford, California, February 11–13, 2019*.
- Zang, A., Stephansson, O., Stenberg, L., Plenkers, K., Specht, S., Milkereit, C., et al. (2017). Hydraulic fracture monitoring in hard rock at 410 m depth with an advanced fluid-injection protocol and extensive sensor array. *Geophysical Journal International*, 208(2), 790–813. <https://doi.org/10.1093/gji/ggw430>
- Zhang, X., Jeffrey, R. G., & Thiercelin, M. (2009). Mechanics of fluid-driven fracture growth in naturally fractured reservoirs with simple network geometries. *Journal of Geophysical Research*, 114, B12406. <https://doi.org/10.1029/2009JB006548>
- Zhang, Y., Doughty, C., Pan, L., Kneafsey, T. J., & The EGS Collab Team. (2018). What could we see at the production well before the thermal breakthrough? Paper presented at *Proceedings 43rd Workshop on Geothermal Reservoir Engineering, Stanford University, Stanford, California* (p. 4).